

Radio Afterglows of Gamma-Ray Bursts and Hypernovae at High Redshift, and their Potential for 21-cm Absorption Studies

Kunihito Ioka¹ and Peter Mészáros^{1,2,3}

¹*Physics Department and Center for Gravitational Wave Physics, Pennsylvania State University, University Park, PA 16802*

²*Department of Astronomy and Astrophysics, Pennsylvania State University, University Park, PA 16802*

³*Institute for Advanced Study, Princeton, NJ 08540*

ABSTRACT

We investigate the radio afterglows of gamma-ray bursts (GRBs) and hypernovae (HNe) at high redshifts and quantify their detectability, as well as their potential usefulness for 21 cm absorption line studies of the intergalactic medium (IGM) and intervening structures. We examine several sets of source and environment model parameters that are physically plausible at high redshifts. The radio afterglows of GRBs would be detectable out to $z \sim 30$, while the energetic HNe could be detectable out to $z \sim 20$ even by the current Very Large Array (VLA). We find that the 21 cm absorption line due to the diffuse neutral IGM is difficult to detect even by the proposed Square Kilometer Array (SKA), except for highly energetic sources. We also find that the 21 cm line due to collapsed gas clouds with high optical depth may be detected on rare occasions.

Subject headings: gamma rays: bursts — intergalactic medium — radio lines: general

1. Introduction

Gamma-Ray Bursts (GRBs) are potentially powerful probes of the early universe (e.g., Miralda-Escudé 1998; Mészáros & Rees 2003; Barkana & Loeb 2004). The substantial evidence that massive stellar collapses lead to long duration GRBs suggests that these outbursts probably occur up to the highest redshifts of the first generation of stars (c.f., Mészáros 2002; Zhang & Mészáros 2003). Their high luminosities make them detectable in principle out to redshifts $z \sim 100$ (Lamb & Reichart 2000), while their afterglows may be observable up

to $z \sim 30$ in the infrared, X-ray (Ciardi & Loeb 2000; Gou, Mészáros, Abel, & Zhang 2004) and radio bands (Ioka 2003; Inoue 2004). About 25% of all GRBs detected by the upcoming Swift satellite are expected to be at $z > 5$ (Bromm & Loeb 2002). Such high redshift GRBs may have already been detected by the BATSE satellite, as suggested by the empirical distance indicators (Fenimore & Ramirez-Ruiz 2000; Norris, Marani, & Bonnell 2000; Murakami et al. 2003; Yonetoku et al. 2004) and their theoretical interpretation (e.g., Ioka & Nakamura 2001; Yamazaki, Ioka, & Nakamura 2004). The first generation of stars are expected to be very massive (Abel, Bryan, & Norman 2002; Bromm, Coppi, & Larson 2002; Omukai & Palla 2003), so that their outcome might be GRBs which are an order of magnitude more luminous than their low redshift counterparts (e.g., Fryer, Woosley, & Heger 2001; Heger et al. 2003).

One of the major uncertainties in modern cosmology is the reionization history of the universe, which has significant implications for the formation of the first stars and their feedback on the subsequent evolution (e.g., Barkana & Loeb 2001; Miralda-Escudé 2003). The analysis of Ly α spectra in the highest redshift quasars indicate that the reionization has essentially reached completion at around $z \sim 6$ (e.g., Fan et al. 2002a), while the WMAP polarization data imply an onset of the reionization process at much higher redshifts $z \sim 17 \pm 5$ (Kogut et al. 2003; Spergel et al. 2003). Although other methods, such as the temperature of the Ly α forest (Theuns et al. 2002; Hui & Haiman 2003), the H_{II} region size around quasars (Wyithe & Loeb 2004; Mesinger & Haiman 2004), and the luminosity function of the Ly α emitters (Stern et al. 2004; Malhotra & Rhoads 2004) also constrain the reionization history, it is still unclear even whether the reionization is a continuous process or whether it occurred in two episodes (Cen 2003; Wyithe & Loeb 2003).

21 cm tomography would be one of the promising ways to reveal the reionization history of the universe¹ (Tozzi et al. 2000; Shaver et al. 1999), by mapping the neutral hydrogen in the spatial and redshift space via the redshifted 21 cm line (Madau, Meiksin, & Rees 1997; Scott & Rees 1990; Hogan & Rees 1979). The 21 cm line is associated with the transition between the singlet and triplet hyperfine levels of the hydrogen atom at the ground state (e.g., Field 1959a). The 21 cm line may be detectable in emission or absorption against the cosmic microwave background (CMB) (e.g., Ciardi & Madau 2003; Furlanetto, Sokasian, & Hernquist 2004; Zaldarriaga, Furlanetto, & Hernquist 2004; Iliev et al. 2002). Alternatively, the 21 cm line may be also observed in absorption against luminous background sources (Carilli, Gnedin, & Owen 2002; Furlanetto & Loeb 2002). But this method requires

¹Other methods using GRBs may include the infrared spectroscopy (Miralda-Escudé 1998; Barkana & Loeb 2004) or photometry (Inoue, Yamazaki, & Nakamura 2004) and the dispersion measure (Ioka 2003; Inoue 2004).

luminous sources of radio continuum at high redshifts, which remain largely speculative. The GRB radio afterglows would be a natural candidate. However their radio fluxes at high redshift have not been estimated in detail. Furlanetto & Loeb (2002) suggested that GRB afterglows are too dim, but they did not explicitly calculate the self-absorption frequencies, nor did they include the reverse shock emission. Another type of related energetic radio source which has not been investigated in this respect are hypernovae (HNe), which may be as frequent as GRBs.

In this paper, we investigate the GRB and HN radio afterglows at high redshifts, including also the possibly of more energetic versions of these objects which may be associated with a population III of stars. We first estimate the maximum redshifts out to which these afterglows could be detected with the Very Large Array (VLA),² Low Frequency Array (LOFAR),³ and Square Kilometer Array (SKA).⁴ This can be important for broadband afterglow fits aimed at determining total energies and physical parameters (e.g., Panaitescu & Kumar 2002) of bursts, out to very high redshifts. We also quantify the detectability of the 21 cm absorption line in the afterglows. Since the afterglow model parameters, such as the energy and duration of the GRBs as well as the ambient density may be different at high redshifts, we examine several possibilities of the model parameters. However, even with the SKA, which has the best sensitivity among the proposed telescopes, and with our improved spectral-temporal evolution model, we find that the chances are low for the detection of 21 cm absorption lines from GRBs and HNe, except in the case of exceptionally energetic sources. This quantification exercise should be useful for the assessment and planning of future observing projects with advanced facilities and detectors.

The paper is organized as follows. In § 2, we calculate the GRB and HN radio afterglows at high redshift, based on the afterglow model summarized in § A. By comparing the afterglow fluxes with the VLA, LOFAR and SKA sensitivities, we discuss the maximum redshift out to which the radio afterglow of these sources would be detectable. We calculate the 21 cm line absorption in the IGM and intervening structures at $z \gtrsim 6$ in § 3 and at $z \lesssim 6$ in § 4. Our conclusions are summarized in § 5. Throughout the paper we use a Λ CDM cosmology with $(\Omega_m, \Omega_\Lambda, \Omega_b, h) = (0.27, 0.73, 0.044, 0.71)$ (Spergel et al. 2003).

²<http://www.nrao.edu/>

³<http://www.lofar.org/>

⁴<http://www.skatelescope.org/>

2. Radio fluxes of high redshift afterglows

We model the GRB afterglow source as a relativistic shell expanding into a homogeneous interstellar medium (ISM) with particle number density n at redshift z . The shell initially has an isotropic equivalent energy E , a Lorentz factor γ_0 , an opening half-angle θ and a width in the source frame $cT(1+z)^{-1}$, where we assume $\gamma_0^{-1} < \theta$ and the shell width being related to the observed GRB duration T (Kobayashi, Piran, & Sari 1997). The true energy is given by $E_j = \theta^2 E/2$. Two shocks are formed: a forward shock heating the ISM and a reverse shock decelerating the shell. At these shocks electrons are accelerated and magnetic fields are amplified, leading to the synchrotron afterglow emission. We assume that accelerated electrons have a power-law distribution of the Lorentz factor γ_e as $N(\gamma_e)d\gamma_e \propto \gamma_e^{-p}d\gamma_e$ for $\gamma_e > \gamma_m$ (Sari, Piran, & Narayan 1998). We also assume that fractions $\epsilon_{e,f}$ ($\epsilon_{e,r}$) and $\epsilon_{B,f}$ ($\epsilon_{B,r}$) of the shock energy go into electrons and magnetic fields, respectively, at the forward (reverse) shock, where the subscripts f and r indicate the forward and reverse shock, respectively. We also assume adiabatic shocks.

Under the above assumptions, we can calculate the spectra and light curves of the afterglows as summarized in § A. There are 10 model parameters: E , θ , n , p , $\epsilon_{e,f}$, $\epsilon_{B,f}$, $\epsilon_{e,r}$, $\epsilon_{B,r}$, γ_0 , $T/(1+z)$, but we assume $\epsilon_{e,f} = \epsilon_{e,r}$ for simplicity, so the actual number of parameters is 9. We consider the possible difference between the magnetic field in the forward and reverse shocks, by using $\mathcal{R}_B = (\epsilon_{B,r}/\epsilon_{B,f})^{1/2}$ in equation (A24) instead of $\epsilon_{B,r}$, since the ejected shell may be endowed with magnetic fields from the central source (e.g., Zhang, Kobayashi, & Mészáros 2003). We also take the sideways expansion of the jet, the non-relativistic regime, and the reverse shock emission into account (see § A).

In the following we examine several sets of model parameters that are physically motivated at high redshift, as summarized in Table 1. We estimate the maximum redshift out to which these afterglows could be detected with the VLA, LOFAR and SKA. We also evaluate the peak fluxes of the afterglows at the observed frequency around $\nu \sim 100$ MHz to discuss the detectability of the 21 cm absorption line later in § 3 and § 4.

2.1. Standard GRB case

First we adopt typical parameters inferred from the broadband afterglow fitting (e.g., Panaitescu & Kumar 2002; Zhang, Kobayashi, & Mészáros 2003): the isotropic equivalent energy $E = 10^{53}$ erg, the opening half-angle $\theta = 0.1$, the ISM density $n = 0.1 \text{ cm}^{-3}$, the spectral index $p = 2.2$, the initial Lorentz factor $\gamma_0 = 200$, the duration in the source frame $T/(1+z) = 10$ s, and the plasma parameters $\epsilon_e = 0.1$, $\epsilon_B = 0.01$, $\mathcal{R}_B = 1$.

Figure 1 shows the total fluxes of the forward and reverse shock emission at the observed frequency $\nu = 5$ GHz and the observed times, $t = 1$ hr, 1 day, 10 days and 100 days, as a function of redshift z . The 5σ sensitivities of the VLA and SKA are also shown. We can see that the radio afterglows can be detected up to $z \sim 30$ even by the current VLA. Here we use the sensitivity,

$$F_{\nu}^{\text{sen}} = \frac{\text{SNR} \cdot 2kT_{\text{sys}}}{A_{\text{eff}}\sqrt{2t_{\text{int}}\Delta\nu}} \sim 23\mu\text{Jy} \left(\frac{\text{SNR}}{5}\right) \left(\frac{2 \times 10^6 \text{cm}^2 \text{K}^{-1}}{A_{\text{eff}}/T_{\text{sys}}}\right) \left(\frac{1\text{day}}{t_{\text{int}}}\right)^{1/2} \left(\frac{50\text{MHz}}{\Delta\nu}\right)^{1/2}, \quad (1)$$

assuming the signal-to-noise ratio (SNR) 5, the integration time $t_{\text{int}} = 1$ day, the band width $\Delta\nu = 50$ MHz, $A_{\text{eff}}/T_{\text{sys}} \sim 2 \times 10^6 \text{cm}^{-2} \text{K}^{-1}$ for the VLA, and $A_{\text{eff}}/T_{\text{sys}} \sim 2 \times 10^8 \text{cm}^{-2} \text{K}^{-1}$ for the SKA. Note that LOFAR will have the frequency range from ~ 10 to ~ 250 MHz, and not at ~ 5 GHz. In Figure 1, the forward shock emission usually dominates the reverse shock one. We can also see that the redshift dependence is rather weak.

Figure 2 shows the light curves of the standard GRB afterglows at $z = 6$ and $\nu \sim 200$ MHz and at $z = 13$ and $\nu \sim 100$ MHz, which correspond to the redshifted 21 cm band. The 5σ sensitivities of the VLA, LOFAR and SKA are also shown. We see that LOFAR and SKA can detect the standard afterglows at low frequencies ~ 100 MHz and high redshift $z \sim 10$, but it may be difficult to detect them with the VLA. Here we assumed an integration time of one-third of the observed time t , a band width $\Delta\nu = 50$ MHz, $A_{\text{eff}}/T_{\text{sys}} \sim 3 \times 10^5 \text{cm}^{-2} \text{K}^{-1}$ for the VLA, $A_{\text{eff}}/T_{\text{sys}} \sim 4 \times 10^6 \text{cm}^{-2} \text{K}^{-1}$ for the LOFAR, and $A_{\text{eff}}/T_{\text{sys}} \sim 5 \times 10^7 \text{cm}^{-2} \text{K}^{-1}$ for the SKA. Note that $A_{\text{eff}}/T_{\text{sys}}$ at ~ 100 MHz is lower than that at ~ 5 GHz because of the galactic background.

From Figure 2 one sees that the peak flux is about $\sim 1\text{-}10 \mu\text{Jy}$ at the redshifted frequency of the 21 cm line, $\nu = 1420/(1+z)$ MHz, for $z \gtrsim 6$. At these frequencies, the forward shock is brighter than the reverse shock, and the dependence on the redshift is rather weak. For most of the time the afterglow flux is below the self-absorption frequency ν_a , so the flux is limited by the blackbody value in equation (A20). Since the flux is proportional to the electron temperature and the reverse shock has lower temperature than the forward shock, the reverse shock is dimmer than the forward shock for our parameters. The first break in the forward shock emission at $t \sim 10^{-2}$ day corresponds to the shock crossing time t_{\times} in equation (A2), the second break at $t \sim 10$ day corresponds to the jet break time t_{θ} in equation (A8), the third break at $t \sim 10^2$ day is due to the characteristic synchrotron frequency $\nu_{m,f}$ crossing the observed frequency ν , the final peak is due to the self-absorption frequency $\nu_{a,f}$ crossing the observed frequency ν , and the non-relativistic phase begins soon after the final peak (see § A). The self-absorbed flux depends on the density as $F_{\nu,\text{BB}} \propto n^{-1/2}$

at $t_x < t < t_\theta$ if $\nu < \nu_{m,f} < \nu_{c,f}$ from equation (A20). Thus the flux is higher for a lower density. However, if the density is too low, the synchrotron flux in equations (A14) and (A15) falls below the blackbody flux in equation (A20) and the observed flux decreases as the density decreases, since $F_{\nu,\text{max},f} \propto n^{1/2}$ at $t_x < t < t_\theta$ if $\nu < \nu_{m,f} < \nu_{c,f}$. We find that the flux is maximized at $n \sim 10^{-2} \text{ cm}^{-3}$ for our parameters (see also § 2.3).

2.2. Energetic GRB case

The first generation of stars are expected to be metal-free and very massive (Abel, Bryan, & Norman 2002; Bromm, Coppi, & Larson 2002; Omukai & Palla 2003). If the collapse of some of these population III stars leads to the launch of relativistic jets, they could lead to an order of magnitude more energetic GRBs than their low redshift counterparts (e.g., Mészáros & Rees 2003; Fryer, Woosley, & Heger 2001; Heger et al. 2003). Here we study a hypothesized energetic GRB case with isotropic equivalent energy $E = 10^{54}$ erg, fixing the other parameters as in the standard case.

Figure 3 shows the total fluxes of the forward and reverse shock emission at the observed frequency $\nu = 5$ GHz and the observed times, $t = 1$ hr, 1 day, 10 days and 100 days, as a function of redshift z , together with the 5σ sensitivities of the VLA and SKA. By comparing Figures 3 and 1 we see that the detection is easier than in the standard case, and even the VLA could easily detect such energetic GRB afterglows beyond $z \sim 30$.

Figure 4 shows the light curves of the energetic GRB afterglows at $z = 6$ and $\nu \sim 200$ MHz, and at $z = 13$ and $\nu \sim 100$ MHz. The 5σ sensitivities of the VLA, LOFAR and SKA are also shown. This indicates that LOFAR and SKA can detect such energetic afterglows at low frequencies ~ 100 MHz and high redshift $z \sim 10$, while VLA may detect them if observed for a long enough time. The predicted peak flux is about $\sim 10\text{-}10^2 \mu\text{Jy}$ at the redshifted 21 cm frequency, $\nu = 1420/(1+z)$ MHz, for $z \gtrsim 6$.

2.3. High density external medium case

Even at high redshifts, the ambient density into which the shell expands could be low, $n \lesssim 1 \text{ cm}^{-3}$ as assumed in the standard case (§ 2.1), since the strong radiation from the progenitor star may evacuate a cavity in the surrounding gas (Whalen, Abel, & Norman 2004; Kitayama et al. 2004). If this does not happen, however, the external density could be higher at high redshifts, based on hierarchical structure formation scenarios. The predicted evolution may be, e.g., $n \propto (1+z)^4$ for a fixed host galaxy mass (Ciardi & Loeb

2000). Since little is known observationally about the ambient density at high redshifts, we assume a nominal high density case with $n = 10^2 \text{ cm}^{-2}$. Other parameters are the same as the standard case.

Figure 5 shows the total fluxes of the forward and reverse shock emission at the observed frequency $\nu = 5 \text{ GHz}$ and the observed times $t = 1 \text{ hr}$, 1 day , 10 days and 100 days , as a function of redshift z , together with the 5σ sensitivities of the VLA and SKA. By comparing Figures 5 and 1 we can see that the detection at this frequency is easier than in the standard case, and even the VLA can easily detect such high density GRB afterglows beyond $z \sim 30$.

Figure 6 shows the light curves of the high density GRB afterglows at $z = 6$ and $\nu \sim 200 \text{ MHz}$ and at $z = 13$ and $\nu \sim 100 \text{ MHz}$. The 5σ sensitivities of the VLA, LOFAR and SKA are also shown. This shows that the detection of the high density GRB afterglows at low frequencies $\sim 100 \text{ MHz}$ and high redshift $z \sim 10$ is difficult. Even the SKA would require very long observing times. The flux is dimmer than in the standard case in Figure 2, because the self-absorption strongly suppresses the low frequency fluxes in this high density case. From Figure 6, we see that the peak flux is about $\sim 10^{-1} \mu\text{Jy}$ at the redshifted 21 cm frequency, $\nu = 1420/(1+z) \text{ MHz}$, for $z \gtrsim 6$.

2.4. Long duration GRB case

The GRB duration at high redshifts could in principle be much longer than at low redshifts, since more massive progenitor stars could lead to longer accretion times and longer jet feeding times (Fryer, Woosley, & Heger 2001). A long duration may also be due to continued fallback of material when the explosion is too mild (MacFadyen, Woosley, & Heger 2001). BATSE did detect a few bursts longer than 1000 s , with its standard peak-flux trigger, instead of a fluence trigger. Swift has the ability to operate with a fluence trigger, which potentially could lead to the detection of longer GRBs. As an example of long duration GRBs, we investigate a case whose duration in the source frame is $T/(1+z) = 1000 \text{ s}$. Other parameters are the same as in the standard case.

Figure 7 shows the total fluxes of the forward and reverse shock emission at an observed frequency $\nu = 5 \text{ GHz}$ and at observed times, $t = 1 \text{ hr}$, 1 day , 10 days and 100 days , as a function of redshift z , together with the 5σ sensitivities of the VLA and SKA. Comparing Figures 7 and 1 we see that the detection of long bursts is easier than for the standard case of duration $T/(1+z) = 10 \text{ s}$, and even the VLA can easily detect such long burst afterglows beyond $z \sim 30$. This is because the reverse shock emission at early times $t \lesssim 10 \text{ day}$ is enhanced due to the long duration.

Figure 8 shows the long duration GRB afterglow light curves at $z = 6$ and $\nu \sim 200$ MHz and at $z = 13$ and $\nu \sim 100$ MHz. The 5σ sensitivities of the VLA, LOFAR and SKA are also shown. Although the reverse shock emission is brighter than in the standard case in Figure 2, it is still below the forward shock emission at low frequencies ~ 100 MHz. Since the forward shock emission is similar to the standard case, the detectability at these frequencies is similar to the standard case. LOFAR and SKA should be able to detect the long duration GRB afterglows at low frequencies ~ 100 MHz and high redshift $z \sim 10$, while it appears difficult for the VLA to detect them. As seen in Figure 8, the peak flux is about $\sim 1\text{-}10 \mu\text{Jy}$ at the redshifted 21 cm frequency, $\nu = 1420/(1+z)$ MHz, for $z \gtrsim 6$.

2.5. Magnetized GRB ejecta case

Several observations suggest that the ejected shell may be strongly magnetized. A large linear polarization in the gamma-ray emission of GRB 021206 has been interpreted as implying a uniform ordered magnetic field over the visible region (Coburn & Boggs 2003), which could be a magnetic field advected from the central source (see however Rutledge & Fox 2004; Wigger et al. 2004). The early afterglows of GRB 990123 and GRB 021211 also may imply that the reverse shock region has a stronger magnetic field than the forward shock region (Zhang, Kobayashi, & Mészáros 2003; Fan et al. 2002b). Although further studies are necessary to verify these suggestions (e.g., Zhang & Kobayashi 2004; Matsumiya & Ioka 2003; Fan, Wei, & Wang 2004), it is useful to examine as a possibility the strongly magnetized case. Here we adopt a ratio of reverse to forward magnetic field strengths $\mathcal{R}_B = 5$, with the other parameters the same as in the standard case.

Figure 9 shows the total fluxes of the forward and reverse shock emission at the observed frequency $\nu = 5$ GHz for observed times $t = 1$ hr, 1 day, 10 days and 100 days, as a function of redshift z , together with the 5σ sensitivities of the VLA and SKA. Comparing Figures 9 and 1 we see that the detection of the magnetized GRB afterglow is somewhat easier than for the standard case, and even the current VLA could detect such magnetized GRB afterglows up to $z \sim 30$. A small increase in the flux is caused by the reverse shock emission at early times $t \lesssim 10$ day, due to the higher reverse magnetic field.

Figure 10 shows the light curves of the magnetized GRB afterglows at $z = 6$ and $\nu \sim 200$ MHz and at $z = 13$ and $\nu \sim 100$ MHz. The 5σ sensitivities of the VLA, LOFAR and SKA are also shown. The reverse shock emission at low frequencies ~ 100 MHz is still below the forward shock emission, being dimmer at these frequencies than in the standard case in Figure 2. Since the forward shock emission is similar to the standard case, the detectability is similar to that in the standard case. We see that LOFAR and SKA can detect the magnetized

afterglows at low frequencies ~ 100 MHz and high redshift $z \sim 10$, while the VLA may have difficulty detecting them. From Figure 10, the peak flux is seen to be about $\sim 1\text{-}10 \mu\text{Jy}$ at the redshifted 21 cm frequency, $\nu = 1420/(1+z)$ MHz, for $z \gtrsim 6$.

2.6. Hypernova radio afterglow

The association of Type Ib/c supernovae (SNe) with GRBs has confirmed the massive stellar origin of long GRBs (e.g., Zhang & Mészáros 2003; Mészáros 2002). Only a small fraction of core collapse SNe appear to lead to GRB jets with high Lorentz factor $\gamma_0 \gtrsim 100$ (Berger et al. 2003; Soderberg, Frail, & Wieringa 2004). However, there may be a larger number of SNe accompanied by mildly relativistic ejecta, which could in principle involve more energy than typical GRB jets (MacFadyen, Woosley, & Heger 2001; Granot & Ramirez-Ruiz 2004). A large kinetic energy $\sim 10^{52}$ erg is also suggested in some core collapse SNe, by the optical light curve and spectral fits (Nomoto et al. 2003; Podsiadlowski et al. 2004), and these objects appear in a number of cases not to be associated with detected GRB. Such energetic supernovae (or hypernovae, HNe) may be powered by jets that fail to bore their way through the stellar envelope (Khokhlov et al. 1999; Mészáros & Rees 2001). At high redshifts, stars are expected to be very massive (Abel, Bryan, & Norman 2002; Bromm, Coppi, & Larson 2002; Omukai & Palla 2003), and it may be more frequent for the jet to be choked even while the jet could be ~ 10 times more energetic (Heger et al. 2003; Fryer, Woosley, & Heger 2001).

Based on these considerations, an isotropic equivalent energy of $E \sim 10^{53}$ erg may be reasonable for high redshift HNe, and depending on the energy conversion efficiency, even an isotropic equivalent energy of $E \sim 10^{54}$ erg may not be implausible for population III HNe (Fryer, Woosley, & Heger 2001; Heger et al. 2003). Keeping in mind the hypothetical nature of this assumption, we examine an extreme HNe afterglow case with isotropic equivalent energy $E = 10^{54}$ erg, ejecta opening half-angle $\theta = 1/\sqrt{2}$ (nearly spherical) and initial Lorentz factor $\gamma_0 = 2$ (mildly relativistic). Other parameters are the same as in the standard GRB case. We note that different authors define HNe differently. Here, our definition of HNe is SNe with a large energy and a mildly relativistic ejecta.

Figure 11 shows the total fluxes of the forward and reverse shock emission at the observed frequency $\nu = 5$ GHz and observed times $t = 1$ yr, 3 yrs and 10 yrs, as a function of redshift z , together with the 5σ sensitivities of the VLA and SKA. This shows that the current VLA may be able to detect such energetic HN afterglows up to $z \sim 20$ with ~ 1 day integration times, while SKA can easily detect them beyond $z \sim 30$. We have also calculated a more moderate energy HN case with $E \sim 10^{53}$ erg, as well as a high external density HN case with

$n \sim 10^2 \text{ cm}^{-3}$. The results for these cases (not shown) indicate that the VLA can detect them out to $z \sim 8$ and beyond $z \sim 30$, respectively, while the SKA can easily detect them beyond $z \sim 30$.

Figure 12 shows the light curves of the energetic HN afterglows at $z = 6$ and $\nu \sim 200$ MHz and at $z = 13$ and $\nu \sim 100$ MHz, as well as the 5σ sensitivities of the VLA, LOFAR and SKA. This shows that the VLA, LOFAR and SKA can detect such HN afterglows at low frequencies ~ 100 MHz and high redshifts $z \sim 10$. The peak flux indicated is about $\sim 10^2$ - $10^3 \mu\text{Jy}$ at the redshifted 21 cm frequency, $\nu = 1420/(1+z)$ MHz, for $z \gtrsim 6$. The reverse shock emission is comparable to the forward shock emission, and the redshift dependence is weak. We also calculated the moderate energy HN case $E \sim 10^{53}$ erg and the high density HN case $n \sim 10^2 \text{ cm}^{-3}$ to find that the peak flux at ~ 100 MHz in both cases is about an order of magnitude below the flux in Figure 12.

One caveat about the HN emission is that one may have no prior information about the sky position because of the preponderant lack of detected gamma-ray emission. However the number of HN afterglows at $z \gtrsim 6$ on the sky is estimated as $\sim 10^3 \text{ events yr}^{-1} \times t_{\text{peak}} f_z f_{\text{HN/GRB}} \sim 10^3$, where $t_{\text{peak}} \sim 10^3$ days is the peak time of the HNe, and we assume a fraction $f_z \sim 50 \%$ of all GRBs on the sky originating at $z \gtrsim 6$ (Bromm & Loeb 2002) and a ratio of the HN rate to the GRB one $f_{\text{HN/GRB}} \sim 1$. Thus the imaging of $\sim 40 \text{ deg}^2$ of sky would lead to one HN afterglow at $z \gtrsim 6$, while the field of view of the SKA may be larger than this. Thus, HN afterglows could be detected as a by-product of other related or unrelated observing programs.

It is also interesting to note that the HN afterglows at high redshift may be brighter than their low redshift counterparts, since the energy may be larger at high redshifts and the redshift dependence of the flux is weak when the other parameters are fixed. Thus the orphan afterglow searches (e.g., Totani & Panaitescu 2002) may preferentially find the high redshift afterglows, although the discrimination from variable AGNs may be difficult (Levinson et al. 2002).

3. 21 cm absorption at $z \gtrsim 6$

At redshifts $z \gtrsim 6$ one may expect 21 cm absorption of the radio afterglow emission by the diffuse neutral component of the intergalactic medium (IGM) (Carilli, Gnedin, & Owen 2002), as well as by collapsed gas clouds, such as in minihalos and galactic disks (Furlanetto & Loeb 2002). The 21 cm absorption by the IGM would provide constraints on the reionization history of the universe (Carilli, Gnedin, & Owen 2002), while the 21 cm

forest due to gas clouds would provide information about the structure and galaxy formation at high redshifts. The 21 cm absorption line due to the host galaxy may provide GRB and host galaxy redshifts (Furlanetto & Loeb 2002), independently of other methods such as the Ly α cutoff (Lamb & Reichart 2000) and X-ray lines (Mészáros & Rees 2003; Gou, Mészáros, & Kallman 2004).

We consider first the optical depth of the diffuse IGM to the 21 cm absorption, which is given by

$$\tau = \frac{3c^3 h_P A_{10} n_{\text{HI}}(z)}{32\pi k \nu_0^2 T_S H(z)} = 0.010 \frac{T_{\text{CMB}}}{T_S} \left(\frac{1+z}{10} \right)^{1/2} x_{\text{HI}}, \quad (2)$$

where $T_{\text{CMB}} = 2.73(1+z)$ K is the CMB temperature at redshift z , T_S is the spin temperature of the IGM, x_{HI} is the neutral hydrogen fraction, h_P is Planck's constant, k is Boltzmann's constant, $A_{10} = 2.85 \times 10^{-15} \text{ s}^{-1}$ is the spontaneous emission coefficient of the 21 cm line, $\nu_0 = 1420.4$ MHz is the source frame 21 cm frequency, $H(z) \simeq H_0 \Omega_m^{1/2} (1+z)^{3/2}$ is the Hubble parameter at high z , n_{HI} is the neutral hydrogen density at z , and we assume the helium mass fraction to be 24% (Field 1959a; Madau, Meiksin, & Rees 1997).

The main uncertainty in equation (2) comes from the hydrogen spin temperature T_S . The spin temperature is determined by the gas kinetic temperature T_K and the coupling of T_S with T_K and T_{CMB} (Madau, Meiksin, & Rees 1997; Tozzi et al. 2000). In the presence of only the CMB, we have $T_S \sim T_{\text{CMB}}$. Once the early generation of stars starts emitting Ly α photons, the Ly α pumping may tightly couple the spin temperature with the gas kinetic temperature well before the epoch of full reionization (e.g., Ciardi & Madau 2003). The kinetic temperature drops below the CMB temperature without any heating because of the adiabatic cooling due to the expansion of the universe, while the kinetic temperature may be quickly increased above the CMB temperature by the Ly α and X-ray heating due to the first stars and the shock heating in the high density regions (Carilli, Gnedin, & Owen 2002; Chen & Miralda-Escudé 2004). The uncertainty in the spin temperature is at least $0.5T_{\text{CMB}} \lesssim T_S \lesssim 4T_{\text{CMB}}$ (Chen & Miralda-Escudé 2004). If $T_S \sim 4T_{\text{CMB}}$, the optical depth is about $\tau \sim 0.0021x_{\text{HI}}$ at $z \sim 6$ and $\tau \sim 0.0030x_{\text{HI}}$ at $z \sim 13$ from equation (2).

In order to detect the 21 cm absorption line, the source flux should be larger than

$$F_\nu^{\text{min}} = \frac{2kT_{\text{sys}}}{A_{\text{eff}} \sqrt{2t\Delta\nu}} \frac{\text{SNR}}{\tau} \\ \sim 1.1 \text{mJy} \left(\frac{\text{SNR}}{5} \right) \left(\frac{0.002}{\tau} \right) \left(\frac{5 \times 10^7 \text{cm}^2 \text{K}^{-1}}{A_{\text{eff}}/T_{\text{sys}}} \right) \left(\frac{10 \text{days}}{t_{\text{int}}} \right)^{1/2} \left(\frac{1 \text{MHz}}{\Delta\nu} \right)^{1/2}, \quad (3)$$

where we assume a band width $\Delta\nu \sim 1$ MHz, an integration time $t_{\text{int}} \sim 10$ days, the SNR 5, the capability of the SKA $A_{\text{eff}}/T_{\text{sys}} \sim 5 \times 10^7 \text{ cm}^2 \text{ K}^{-1}$ at $\nu \sim 200$ MHz, and the small τ limit.

Therefore ~ 1 mJy sources are needed for the detection of the 21 cm absorption due to the diffuse IGM if $T_S \sim 4T_{\text{CMB}}$. If there was an epoch with low spin temperature $T_S \sim 0.5T_{\text{CMB}}$ (Chen & Miralda-Escudé 2004), the required flux could be as low as ~ 0.1 mJy, since $\tau \propto T_S^{-1}$ from equation (2). Note that the redshift is determined with the precision,

$$\Delta z \sim \frac{\Delta\nu(1+z)^2}{\nu_0} \sim 0.070 \left(\frac{1+z}{10} \right)^2 \left(\frac{\Delta\nu}{1\text{MHz}} \right), \quad (4)$$

for the band width $\Delta\nu \sim 1$ MHz. Note also that the LOFAR will have $A_{\text{eff}}/T_{\text{sys}} \sim 4 \times 10^6$ cm² K⁻¹ at $\nu \sim 100$ MHz, so that the required flux is ~ 10 times larger than that for the SKA.

Comparing the minimum flux F_ν^{min} of equation (3) with the peak fluxes of the afterglows in Figures 2, 4, 6, 8, 10 and 12, we see that in almost all cases there is little or no chance to detect the 21 cm line due to the diffuse IGM. The only one exception is the hypothetical energetic HN case with isotropic equivalent energy $E \sim 10^{54}$ erg in a low ambient density $n \lesssim 1$ cm⁻³, if the HN occurs at an epoch with low spin temperature $T_S \lesssim 0.5T_{\text{CMB}}$. Although such a HN is not implausible, there is so far no evidence for it. We conclude that it is likely to be difficult to detect 21 cm absorption due to the diffuse IGM in the afterglows discussed here with the currently existing or envisaged telescopes. Such detections may require a telescope with $\sim 10 - 100$ times better sensitivity than the SKA.

The 21 cm absorption due to collapsed gas clouds may have better detection prospects, since the optical depth can be high, $\tau \gtrsim 1$, because of the high density contrast. The number of clouds with optical depth larger than unity $\tau \gtrsim 1$ may be 0.01-0.1 per redshift, while some of host galaxies may have $\tau \gtrsim 1$ (Furlanetto & Loeb 2002). In order to resolve the clouds, the bandwidth should be narrower than the line width, which is about

$$\Delta\nu \sim 3.9 \left(\frac{T_S}{10^3\text{K}} \right)^{1/2} \left(\frac{1+z}{10} \right)^{-1} \text{ kHz}, \quad (5)$$

if the line width is determined by the spin temperature. We note that a spin temperature of order $T_S \sim 10^3$ K is measured in several damped Ly α systems at low redshift, while it may be higher at high redshift (Kanekar & Chengalur 2003). If we adopt $\Delta\nu \sim 10$ kHz and $\tau \gtrsim 1$, the required minimum source flux is about ~ 0.02 mJy from equation (3). Then the 21 cm absorption line due to gas clouds may be detected in the energetic HN case, as we can see from Figure 12, while from Figures 2, 4, 6, 8 and 10, it could be marginally detected in the other afterglow cases if the ambient density is low $n \lesssim 1$ cm⁻³.

4. 21 cm absorption at $z \lesssim 6$

At redshifts $z \lesssim 6$, 21 cm absorption is expected predominantly from neutral gas clouds observed as damped Ly α systems, rather than from the diffuse IGM, since the latter is almost completely ionized. The optical depth of damped Ly α systems with the comoving H $_I$ column density N_{H_I} and the spin temperature T_S is about

$$\tau = \frac{3c^2 h_{\text{P}} A_{10} N_{\text{H}_I}}{32\pi k \nu_0 T_S \Delta\nu_c} \sim 6.7 \left(\frac{N_{\text{H}_I}}{10^{23} \text{cm}^{-2}} \right) \left(\frac{T_S}{10^3 \text{K}} \right)^{-3/2}, \quad (6)$$

where we assumed a comoving line width $\Delta\nu_c = (1+z)\Delta\nu = 39(T_S/10^3\text{K})^{1/2}$ kHz as in equation (5) (Field 1959a). Thus the optical depth is larger than unity, $\tau \gtrsim 1$, for an H $_I$ column density $N_{\text{H}_I} \gtrsim 3 \times 10^{22} (T_S/10^3\text{K})^{3/2} \text{cm}^{-2}$. The spin temperature of order $T_S \sim 10^3$ K is motivated again on the damped Ly α system data and discussion of Kanekar & Chengalur (2003).

As in the previous section, if we adopt $\Delta\nu \sim 10$ kHz and $\tau \gtrsim 1$, the required source flux is about ~ 0.02 mJy from equation (3). Thus, the 21 cm line due to the damped Ly α systems may be detected in the energetic HN case, as we see from Figure 12, while it could be marginally detected in the other afterglow cases if the ambient density is low $n \lesssim 1 \text{cm}^{-3}$, from Figures 2, 4, 6, 8 and 10. Note that the detection of the 21 cm line at $z \lesssim 6$ is less difficult than at $z \gtrsim 6$, since the observed 21 cm frequency is higher at lower redshifts, and the self-absorbed spectrum of the afterglows has a steep rising form, $F_\nu \propto \nu^2$ or $F_\nu \propto \nu^{5/2}$, in equation (A20).

The number of absorption lines per unit redshift and unit comoving H $_I$ density is estimated from observations of the Ly α systems as

$$\frac{\partial^2 N}{\partial z \partial N_{\text{H}_I}} \sim C_{\text{H}_I} N_{\text{H}_I}^{-\lambda}, \quad (7)$$

where $C_{\text{H}_I} \sim 10^{5.2}$ and $\lambda \sim 1.33$ (e.g., Penton, Stocke, & Shull 2004), and the redshift evolution does not seem to be strong (e.g., Storrie-Lombardi & Wolfe 2000). Therefore the number of the 21 cm line with optical depth larger than unity $\tau \gtrsim 1$ is about $\sim 0.006 (T_S/10^3\text{K})^{3(1-\lambda)/2}$ per redshift. Since an integration time of order $t_{\text{int}} \sim 10$ days is necessary even for $\tau \sim 1$ clouds, we conclude that it may be difficult to detect the 21 cm line due to the damped Ly α clouds in the $z \lesssim 6$ range.

5. Conclusions

We have investigated the radio afterglows of GRBs and HNe at high redshifts, analyzing their detectability as well as their possible usefulness for 21 cm absorption measurements. We explored several possible sets of model parameters which are plausible at high redshifts (see Table 1). Our source models include the effects associated with reverse as well as forward shock emission, jet breaks and sideways expansion of the jet, and the transition from a relativistic to non-relativistic expansion regime.

Our results indicate that standard GRB radio afterglows may be detected with the current VLA up to $z \sim 30$, and energetic HN afterglows may be detected up to $z \sim 20$, at high radio frequencies ~ 5 GHz. The proposed SKA should be easily able to detect the GRB and HN afterglows beyond $z \sim 30$ at frequencies ~ 5 GHz. Other possible effects which may be expected at high redshift, such as a larger isotropic equivalent energy, higher external density, longer duration GRB and the possibility of magnetized ejecta, can all contribute to enhance the detectability of afterglows at ~ 5 GHz.

We find that it is difficult to detect the 21 cm absorption line due to a diffuse neutral IGM, even with the SKA. A possible exception may be in the case of a very high isotropic equivalent HN energy $E \sim 10^{54}$ erg, if it occurs in a low ambient density $n \lesssim 1 \text{ cm}^{-3}$ at an epoch with low spin temperature $T_S \lesssim 0.5T_{\text{CMB}}$. This case is very hypothetical, but could be plausible under some conditions.

The 21 cm absorption from collapsed gas clouds along the line of sight, e.g., from minihalos and galactic disks at $z \gtrsim 6$ and damped Ly α systems at $z \lesssim 6$, is in principle detectable in the energetic HN case, and marginally detectable in the GRB afterglow cases considered, if the 21 cm optical depth of the clouds is larger than unity and the ambient gas density of the GRBs is low, $n \lesssim 1 \text{ cm}^{-3}$. However, such high optical depth gas clouds are rare, and their detection is not practical given the long integration times needed. This indicates that if 21 cm absorption is detected in a narrow range of frequencies, it is likely to originate in the host galaxy of the GRB or HN with a high 21 cm optical depth, e.g., in an edge-on disk, star-forming galaxy or protogalaxy, and may thus provide a direct measurement of the redshift of the host.

We thank M.J. Rees and S. Kobayashi for useful discussions. This work was supported in part by the Eberly Research Funds of Penn State and by the Center for Gravitational Wave Physics under grants PHY-01-14375 (KI), NASA NAG5-13286, NSF AST 0098416 and the Monell Foundation.

A. Afterglow model

We summarize the afterglow model in this section (c.f., Zhang & Mészáros 2003; Mészáros 2002). § A.1 is for the forward shock, while § A.2 is for the reverse shock. A very early evolution of the reverse shock emission is derived in § A.3. We will neglect the inverse Compton cooling since almost all phase is in the slow cooling (Sari & Esin 2001). We will also neglect the effects of the dispersion delay, the free-free absorption, and the scintillation (e.g., Ioka 2003).

The afterglow evolution is divided into two classes depending on the shell width $cT(1+z)^{-1}$ (Sari & Piran 1995). We consider that the shell is thin (thick) if $T < t_\gamma$ ($t_\gamma < T$) where

$$t_\gamma = \frac{1+z}{4\gamma_0^2 c} \left(\frac{3E}{4\pi\gamma_0^2 n m_p c^2} \right)^{1/3} \sim 100 E_{53}^{1/3} \gamma_{0,2}^{-8/3} n^{-1/3} (1+z) \text{ s} \quad (\text{A1})$$

is the observed time for the forward shock to collect $\sim \gamma_0^{-1}$ of the shell's rest mass, $E = 10^{53} E_{53}$ erg and $\gamma_0 = 10^2 \gamma_{0,2}$. The evolution becomes independent of the shell thickness in a self-similar manner after the shock crosses the shell at

$$t_\times = \max(t_\gamma, T), \quad (\text{A2})$$

where the first (second) value in the bracket is for the thin (thick) case (Kobayashi & Sari 2000). The evolution is also independent of the shell width in the very beginning before the time

$$t_i = \min(T, t_N), \quad (\text{A3})$$

where the first (second) value in the bracket is for the thin (thick) case,

$$t_N = \frac{1+z}{4\gamma_0^2 c} \left[\frac{3E(1+z)}{16\pi n m_p c^3 T \gamma_0^4} \right]^{1/2} \sim 100 E_{53}^{1/2} \gamma_{0,2}^{-4} n^{-1/2} T_2^{-1/2} \text{ s} \quad (\text{A4})$$

is the time for the reverse shock to be relativistic, and $T = 10^2 T_2$ corresponds to the spreading time of the shell (Sari & Piran 1995). Thus the evolution depends on the shell width in the interval $t_i < t < t_\times$.

A.1. Forward shock

First let us consider the forward shock. We may divide the problem into two parts: dynamics and radiation.

Dynamics: In the beginning $t < t_i$, the swept mass is too small to affect the system and the Lorentz factor is constant,

$$\gamma(t) \sim \gamma_0, \quad (\text{A5})$$

as functions of the observed time t . In the interval $t_i < t < t_\times$, the Lorentz factor is still constant for thin shells, $\gamma(t) \sim \gamma_0$, while the deceleration begins for thick shells,

$$\gamma(t) \sim \gamma_0(t/t_N)^{-1/4}, \quad (\text{A6})$$

since the reverse shock becomes relativistic (Sari & Piran 1995; Sari 1997). After entering the self-similar phase, $t_\times < t$, the hydrodynamics is determined by the adiabatic condition $E \sim 4\pi\gamma^2 R^3 n m_p c^2 / 3$ and the relation $R \sim 4\gamma^2 ct / (1+z)$ in equation (A13) as

$$\gamma(t) \sim [3E(1+z)^3 / 256\pi n m_p c^5 t^3]^{1/8}, \quad (\text{A7})$$

irrespective of the shell width. The Lorentz factor drops below θ^{-1} around the time

$$t_\theta \sim \frac{1+z}{4\theta^{-2}c} R_\theta \sim 5 \times 10^4 E_{53}^{1/3} \theta_{-1}^{8/3} n^{-1/3} (1+z) \text{ s}, \quad (\text{A8})$$

where

$$R_\theta \sim (3E\theta^2 / 4\pi n m_p c^2)^{1/3}. \quad (\text{A9})$$

Then the jet starts to expand sideways (Rhoads 1999; Sari, Piran, & Halpern 1999), so that the dynamics changes as

$$\gamma(t) \sim \theta^{-1}(t/t_\theta)^{-1/2}. \quad (\text{A10})$$

Finally the shock velocity becomes non-relativistic (Waxman, Kulkarni, & Frail 1998; Frail, Waxman, & Kulkarni 2000) around the time

$$t_{NR} = \frac{1+z}{4\gamma_{NR}^2 c} R_\theta \sim 2 \times 10^6 E_{52}^{1/3} \theta_{-1}^{2/3} n^{-1/3} (1+z) \text{ s}, \quad (\text{A11})$$

where $\gamma_{NR} = (1 - \beta_{NR}^2)^{-1/2}$ and we adopt the non-relativistic velocity $\beta_{NR} = 2^{-1/2}$. The flow becomes nearly spherical, so that the dynamics is described by the self-similar Sedov solution as

$$\beta(t) \sim \beta_{NR}(t/t_{NR})^{-3/5}. \quad (\text{A12})$$

For simplicity we use the shock radius given by

$$R(t) \sim 4[\gamma(t)]^2 ct / (1+z), \quad (\text{A13})$$

for the relativistic case (Sari 1998; Waxman 1997; Panaitescu & Mészáros 1998), while $R(t) \propto \beta(t)t$ for the non-relativistic case.

Radiation: Once the dynamics above determine $\gamma(t)$ and $R(t)$, we may estimate the synchrotron spectrum as follows. The synchrotron spectrum from relativistic electrons in a power-law distribution usually has four power-law segments with three breaks at the self-absorption frequency $\nu_{a,f}$, the characteristic synchrotron frequency $\nu_{m,f}$, and the cooling frequency $\nu_{c,f}$ (Sari, Piran, & Narayan 1998). If we temporarily neglect the self-absorption, the observed flux is given by

$$F_{\nu,f} = \begin{cases} (\nu/\nu_{m,f})^{1/3} F_{\nu,\max,f}, & \nu < \nu_{m,f}, \\ (\nu/\nu_{m,f})^{-(p-1)/2} F_{\nu,\max,f}, & \nu_{m,f} < \nu < \nu_{c,f}, \\ (\nu_{c,f}/\nu_{m,f})^{-(p-1)/2} (\nu/\nu_{c,f})^{-p/2} F_{\nu,\max,f}, & \nu_{c,f} < \nu, \end{cases} \quad (\text{A14})$$

in the slow cooling case $\nu_{m,f} < \nu_{c,f}$, and

$$F_{\nu,f} = \begin{cases} (\nu/\nu_{c,f})^{1/3} F_{\nu,\max,f}, & \nu < \nu_{c,f}, \\ (\nu/\nu_{c,f})^{-1/2} F_{\nu,\max,f}, & \nu_{c,f} < \nu < \nu_{m,f}, \\ (\nu_{m,f}/\nu_{c,f})^{-1/2} (\nu/\nu_{m,f})^{-p/2} F_{\nu,\max,f}, & \nu_{m,f} < \nu, \end{cases} \quad (\text{A15})$$

in the fast cooling case $\nu_{c,f} < \nu_{m,f}$, where

$$F_{\nu,\max,f} = \frac{\sigma_T m_e c^2}{9q_e} \frac{R^3 n B_f \gamma (1+z)}{D^2} \quad (\text{A16})$$

is the observed peak flux at the luminosity distance $D = (1+z) \int_0^z (1+z) |dt/dz| dz$ with $|dt/dz|^{-1} = (1+z) H_0 [\Omega_m (1+z)^3 + \Omega_\Lambda]^{1/2}$, and

$$B_f = [32\pi m_p \epsilon_{B,f} n \gamma (\gamma - 1)]^{1/2} c, \quad (\text{A17})$$

is the comoving magnetic field. The characteristic synchrotron frequency $\nu_{m,f}$ and the cooling frequency $\nu_{c,f}$ are given by $\nu(\gamma_{m,f})$ and $\nu(\gamma_{c,f})$, respectively, where

$$\nu(\gamma_e) = \frac{\gamma \gamma_e^2 q_e B}{2\pi m_e c (1+z)}, \quad (\text{A18})$$

is the frequency at which electrons with the Lorentz factor γ_e radiate, and

$$\gamma_{m,f} = \epsilon_{e,f} \frac{p-2}{p-1} \frac{m_p}{m_e} (\gamma - 1), \quad \gamma_{c,f} = \frac{6\pi m_e c (1+z)}{\sigma_T \gamma B_f^2 t}. \quad (\text{A19})$$

Note that we may use B_f and $\gamma_{m,f}$ in equations (A17) and (A19) even in the non-relativistic phase.

The synchrotron self-absorption limits the flux below the blackbody emission with the electron temperature (e.g., Sari & Piran 1999). This is given by

$$F_{\nu,\text{BB}} = 2\pi\nu^2\gamma\gamma_e m_e (R_{\perp}/D)^2(1+z)^3, \quad (\text{A20})$$

where ν is the observed frequency, R_{\perp} is the observed size of the afterglow, and γ_e is the typical Lorentz factor of the electrons emitting at ν . For simplicity we use $R_{\perp}(t) = 4\gamma(t)ct/(1+z)$ for the relativistic case, while $R_{\perp}(t) \propto \beta(t)t$ for the non-relativistic case.

A.2. Reverse shock

Dynamics: In the initial stage $t < t_i$, the Lorentz factor is constant $\gamma \sim \gamma_0$. In the interval $t_i < t < t_{\times}$, we have $\gamma \sim \gamma_0$ for thin shells, while $\gamma \sim \gamma_0(t/t_N)^{-1/4}$ for thick shells. These evolutions are the same as that of the forward shock. After the shell crossing $t_{\times} < t$, the evolution is approximately given by

$$\gamma \sim \gamma_{\times}(t/t_{\times})^{-1/2}, \quad (\text{A21})$$

where $\gamma_{\times} = \min(\gamma_0, \gamma_T)$ is the Lorentz factor at the shell crossing and

$$\gamma_T \sim 100E_{53}^{1/8} n^{-1/8} T_2^{-3/8} (1+z)^{3/8}, \quad (\text{A22})$$

is given by $\gamma(T)$ from equation (A7) (Zhang, Kobayashi, & Mészáros 2003; Kobayashi 2000). A reliable calculation after γ drops below θ^{-1} at $t_{\theta} < t$ requires full numerical simulations and is beyond the scope of this paper. Here we use equation (A21) till the velocity becomes non-relativistic $\gamma \sim \gamma_{NR}$, and use the time dependence of the Sedov solution in equation (A12) after that. Since the evolution in equation (A21) is the same as that of the sideways expansion in equation (A10), this treatment might not be completely wrong. For simplicity we use the shock radius in equation (A13) for all cases.

Radiation: At the shell crossing $t \sim t_{\times}$, the forward and reverse shocks have the same Lorentz factor γ_{\times} , energy density e , and total energy eV . But these shocks have the different relative Lorentz factor across the shock $\bar{\gamma}$, i.e., the forward shock has $\bar{\gamma}_f \sim \gamma_{\times}$ and the reverse shock has $\bar{\gamma}_r \sim \gamma_0/\gamma_{\times}$. These shocks may also have different magnetization parameters $\epsilon_{B,f} \neq \epsilon_{B,r}$ since the ejected shell may carry magnetic fields from the central source (e.g., Zhang, Kobayashi, & Mészáros 2003). Then we can show

$$\frac{\gamma_{m,r}(t_{\times})}{\gamma_{m,f}(t_{\times})} \sim \frac{1}{\hat{\gamma}}, \quad \frac{\gamma_{c,r}(t_{\times})}{\gamma_{c,f}(t_{\times})} \sim \frac{1}{\mathcal{R}_B^2}, \quad (\text{A23})$$

since $\gamma_m \propto \bar{\gamma}$, $\gamma_c \propto \gamma^{-1} B^{-2} t^{-1}$ and $B \propto \epsilon_B e^{1/2}$, where we define

$$\hat{\gamma} = \frac{\gamma_{\times}^2}{\gamma_0}, \quad \mathcal{R}_B = \frac{B_r}{B_f} = \left(\frac{\epsilon_{B,r}}{\epsilon_{B,f}} \right)^{1/2}. \quad (\text{A24})$$

We can also show

$$\frac{\nu_{m,r}(t_{\times})}{\nu_{m,f}(t_{\times})} \sim \frac{\mathcal{R}_B}{\hat{\gamma}^2}, \quad \frac{\nu_{c,r}(t_{\times})}{\nu_{c,f}(t_{\times})} \sim \frac{1}{\mathcal{R}_B^3}, \quad \frac{F_{\nu,\max,r}(t_{\times})}{F_{\nu,\max,f}(t_{\times})} \sim \hat{\gamma} \mathcal{R}_B, \quad (\text{A25})$$

since $\nu_m \propto \gamma B \gamma_m^2$, $\nu_c \propto \gamma^{-1} B^{-3} t^{-2}$, $F_{\nu,\max} \propto \gamma B N_e$ and $N_e \propto eV \bar{\gamma}^{-1}$, where N_e is the total number of emitting electrons.

As in the forward shock case, the synchrotron spectrum is given by equations (A14), (A15) and (A20) replacing the subscript f with r , although the emission above $\nu_{c,r}$ disappears after the shell crossing $t_{\times} < t$ (see below). Thus the light curves can be calculated by specifying the temporal evolutions of ν_m , ν_c and $F_{\nu,\max}$. The evolutions of γ_m and γ_c are also useful for estimating the self-absorption. In the initial stage $t < t_i$, the evolutions are given by

$$\nu_{m,r} \propto t^4, \quad \nu_{c,r} \propto t^{-2}, \quad F_{\nu,\max,r} \propto t^2, \quad (\text{A26})$$

$$\gamma_{m,r} \propto t^2, \quad \gamma_{c,r} \propto t^{-1}, \quad (\text{A27})$$

as shown in § A.3. In the interval $t_i < t < t_{\times}$, thin shells have the dependence

$$\nu_{m,r} \propto t^6, \quad \nu_{c,r} \propto t^{-2}, \quad F_{\nu,\max,r} \propto t^{3/2}, \quad (\text{A28})$$

$$\gamma_{m,r} \propto t^3, \quad \gamma_{c,r} \propto t^{-1}, \quad (\text{A29})$$

while the thick shells have

$$\nu_{m,r} \propto t^0, \quad \nu_{c,r} \propto t^{-1}, \quad F_{\nu,\max,r} \propto t^{1/2}, \quad (\text{A30})$$

$$\gamma_{m,r} \propto t^{1/4}, \quad \gamma_{c,r} \propto t^{-1/4}. \quad (\text{A31})$$

After the shell crossing $t_{\times} < t$, no electron is shocked and electrons only cool adiabatically, so that the evolutions are given by

$$\nu_{m,r} \propto t^{-3/2}, \quad \nu_{c,r} \propto t^{-3/2}, \quad F_{\nu,\max,r} \propto t^{-1}, \quad (\text{A32})$$

$$\gamma_{m,r} \propto t^{-1/4}, \quad \gamma_{c,r} \propto t^{-1/4}, \quad (\text{A33})$$

and the emission above $\nu_{c,r}$ disappears (Zhang, Kobayashi, & Mészáros 2003; Kobayashi 2000; Gou, Mészáros, Abel, & Zhang 2004). In the Sedov phase we use

$$\nu_{m,r} \propto t^{-3}, \quad \nu_{c,r} \propto t^{-3}, \quad F_{\nu,\max,r} \propto t^{-3/5}, \quad (\text{A34})$$

$$\gamma_{m,r} \propto t^{-6/5}, \quad \gamma_{c,r} \propto t^{-6/5}, \quad (\text{A35})$$

by noting that the energy density drops as $\propto \beta^2 \propto t^{-5/6}$.

A.3. Very early reverse shock

Let us derive the evolution of the reverse shock emission in the initial stage $t < t_i$. The evolution is independent of the shell width. The Lorentz factor is constant $\gamma \sim \gamma_0$ since the reverse shock is non-relativistic $\bar{\gamma}_r - 1 \ll 1$ (Sari & Piran 1995). This together with the constant ambient density leads to a constant energy density in the forward and reverse shock $e_r \sim \text{const}$. Since the shell spreading has not started, the shell density decreases as $n_r \propto R^{-2} \propto t^{-2}$. Then the relative velocity across the reverse shock is $\beta_r \propto (\bar{\gamma}_r - 1)^{1/2} \propto e_r^{1/2} n_r^{-1/2} \propto t$, and hence the total number of emitting electrons increases as $N_e \propto \beta_r t \propto t^2$. Recalling $\gamma_m \propto e_r/n_r$, $\gamma_c \propto \gamma^{-1} B^{-2} t^{-1}$ and $B \propto e_r^{1/2}$, we have the time dependence in equation (A27). Similarly we can derive equation (A26) since $\nu_m \propto \gamma B \gamma_m^2$, $\nu_c \propto \gamma^{-1} B^{-3} t^{-2}$ and $F_{\nu, \text{max}} \propto \gamma B N_e$.

REFERENCES

- Abel, T., Bryan, G. L., & Norman, M. L. 2002, *Science*, 295, 93
- Barkana, R., & Loeb, A. 2001, *Phys. Rep.*, 349, 125
- Barkana, R., & Loeb, A. 2004, *ApJ*, 601, 64
- Berger, E., Kulkarni, S. R., Frail, D. A., & Soderberg, A. M. 2003, *ApJ*, 599, 408
- Bromm, V., & Loeb, A. 2002, *ApJ*, 575, 111
- Bromm, V., Coppi, P. S., & Larson, R. B. 2002, *ApJ*, 564, 23
- Carilli, C. L., Gnedin, N. Y., & Owen, F. 2002, *ApJ*, 577, 22
- Cen, R. 2003, *ApJ*, 591, 12
- Chen, X., & Miralda-Escudé, J. 2004, *ApJ*, 602, 1
- Ciardi, B., & Loeb, A. 2000, *ApJ*, 540, 687
- Ciardi, B., & Madau, P. 2003, *ApJ* 596, 1
- Coburn, W., & Boggs, S. E. 2003, *Nature*, 423, 415
- Fan, X., et al. 2002a, *AJ*, 123, 1247
- Fan, Y. Z., Dai, Z. G., Huang, Y. F., & Lu, T. 2002b, *Chin. J. Astron. Astrophysics.*, 2, 449

- Fan, Y. Z., Wei, D. M., & Wang, C. F. 2004, *A&A*, 424, 477
- Fenimore, E. E., & Ramirez-Ruiz, E. 2000, *astro-ph/0004176*
- Field, G. 1959, *ApJ*, 129, 525
- Frail, D. A., Waxman, E., & Kulkarni, S. R. 2000, *ApJ*, 537, 191
- Fryer, C. L., Woosley, S. E., & Heger, A. 2001, *ApJ*, 550, 372
- Furlanetto, S. R., & Loeb, A. 2002, *ApJ*, 579, 1
- Furlanetto, S. R., Sokasian, A., & Hernquist, L. 2004, *MNRAS*, 347, 187
- Gou, L. J., Mészáros, P., Abel, T., & Zhang, B. 2004, *ApJ*, 604, 508
- Gou, L. J., Mészáros, P., & Kallman, T. R. 2004, *astro-ph/0408414*
- Granot, J., & Ramirez-Ruiz, E. 2004, *ApJ*, 609, L9
- Heger, A., Fryer, C. L., Woosley, S. E., Langer, N., & Hartmann, D. H. 2003, *ApJ*, 591, 288
- Hogan, C. J., & Rees, M. J. 1979, *MNRAS*, 188, 791
- Hui, L., & Haiman, Z. 2003, *ApJ*, 596, 9
- Iliev, I. T., Shapiro, P. R., Ferrara, A., & Martel, H. 2002, *ApJ*, 572, L123
- Ioka, K., & Nakamura, T. 2001, *ApJ*, 554, L163
- Ioka, K. 2003, *ApJ*, 598, L79
- Inoue, S. 2004, *MNRAS*, 348, 999
- Inoue, A., Yamazaki, R., & Nakamura, T. 2004, *ApJ*, 601, 644
- Kanekar, N., & Chengalur, J. N. 2003, *A&A*, 399, 857
- Khokhlov, A. M., et al. 1999, *ApJ*, 524, L107
- Kitayama, T., Yoshida, N., Susa, H., & Umemura, M. 2004, *astro-ph/0406280*
- Kobayashi, S. 2000, *ApJ*, 545, 807
- Kobayashi, S., & Sari, R. 2000, *ApJ*, 542, 819
- Kobayashi, S., Piran, T., & Sari, R. 1997, *ApJ*, 490, 92

- Kogut, A., et al. 2003, *ApJS*, 148, 161
- Lamb, D. Q., & Reichart, D. E. 2000, *ApJ*, 536, 1
- Levinson, A., Ofek, E. O., Waxman, E., & Gal-Yam, A. 2002, *ApJ*, 576, 923
- MacFadyen, A. I., Woosley, S. E., & Heger, A. 2001, *ApJ*, 550, 410
- Madau, P., Meiksin, A., & Rees, M. J. 1997, *ApJ*, 475, 429
- Malhotra, S., & Rhoads, J. E. 2004, *astro-ph/0407408*
- Matsumiya, M., & Ioka, K. 2003, *ApJ*, 595, L25
- Mesinger, A., & Haiman, Z. 2004, *ApJ*, 611, L69
- Mészáros, P. 2002, *ARA&A*, 40, 137
- Mészáros, P., & Rees, M. J. 2001, *ApJ*, 556, L37
- Mészáros, P., & Rees, M. J. 2003, *ApJ*, 591, L91
- Miralda-Escudé, J. 1998, *ApJ*, 501, 15
- Miralda-Escudé, J. 2003, *Science*, 300, 1904
- Murakami, T., Yonetoku, D., Izawa, H., & Ioka, K. 2003, *PASJ*, 55, L65
- Nomoto, K., et al. 2003, *astro-ph/0308136*
- Norris, J. P., Marani, G. F., & Bonnell, J. T. 2000, *ApJ*, 534, 248
- Omukai, K., & Palla, F. 2003, *ApJ*, 589, 677
- Panaitescu, A., & Kumar, P. 2002, *ApJ*, 571, 779
- Panaitescu, A., & Mészáros, P. 1998, *ApJ*, 493, L31
- Penton, S. V., Stocke, J. T., & Shull, J. M. 2004, *ApJS*, 152, 29
- Podsiadlowski, P., Mazzali, P. A., Nomoto, K., Lazzati, D., & Cappellaro, E. 2004, *ApJ*, 607, L17
- Rhoads, J. E. 1999, *ApJ*, 525, 737
- Rutledge, R. E., & Fox, D. B. 2004, *MNRAS*, 350, 1288

- Sari, R. 1997, *ApJ*, 489, L37
- Sari, R. 1998, *ApJ*, 494, L49
- Sari, R., & Piran, T. 1995, *ApJ*, 455, L143
- Sari, R., & Piran, T. 1999, *ApJ*, 517, L109
- Sari, R., Piran, T., & Narayan, R. 1998, *ApJ*, 497, L17
- Sari, R., Piran, T., & Halpern, J. P. 1999, *ApJ*, 519, L17
- Sari, R., & Esin, A. A. 2001, *ApJ*, 548, 787
- Scott, D., & Rees, M. J. 1990, *MNRAS*, 247, 510
- Shaver, P. A., Windhorst, R. A., Madau, P., & de Bruyn, A. G. 1999, *A&A*, 345, 380
- Soderberg, A. M., Frail, D. A., & Wieringa, M. H. 2004, *ApJ*, 607, L13
- Spergel, D. N., et al. 2003, *ApJS*, 148, 175
- Stern, D., et al. 2004, *astro-ph/0407409*
- Storrie-Lombardi, L. J., & Wolfe, A. M. 2000, *ApJ*, 543, 552
- Theuns, T., et al. 2002, *ApJ*, 567, L103
- Totani, T., & Panaitescu, A. 2002, *ApJ*, 576, 120
- Tozzi, P., Madau, P., Meiksin, A., & Rees, M. J. 2000, *ApJ*, 528, 597
- Waxman, E. 1997, *ApJ*, 491, L19
- Waxman, E., Kulkarni, S. R., & Frail, D. A. 1998, *ApJ*, 497, 288
- Whalen, D., Abel, T., & Norman, M. L. 2004, *ApJ*, 610, 14
- Wigger, C., Hajdas, W., Arzner, K., Güdel, M., & Zehnder, A. 2004, *ApJ* in press, *astro-ph/0405525*
- Wyithe, J. S. B., & Loeb, A. 2003, *ApJ*, 588, L69
- Wyithe, J. S. B., & Loeb, A. 2004, *Nature*, 427, 815
- Yamazaki, R., Ioka, K., & Nakamura, T. 2004, *ApJ*, 606, L33

Yonetoku, D., Murakami, T., Nakamura, T., Yamazaki, R., Inoue, A. K., & Ioka, K. 2004, *ApJ*, 609, 935

Zaldarriaga, M., Furlanetto, S. R., & Hernquist, L. 2004, *ApJ*, 608, 622

Zhang, B., & Mészáros, P. 2004, *Int. J. Mod. Phys. A*, 19, 2385 (astro-ph/0311321)

Zhang, B., & Kobayashi, S. 2004, astro-ph/0404140

Zhang, B., Kobayashi, S., & Mészáros, P. 2003, *ApJ*, 595, 950

Table 1. Model parameters and some results: the isotropic equivalent energy E erg, the opening half-angle θ , the ISM density n cm $^{-3}$, the spectral index p , the initial Lorentz factor γ_0 , the duration in the source frame $T/(1+z)$ s, the energy fraction of electrons ϵ_e , the energy fraction of magnetic fields ϵ_B , the ratio of reverse to forward magnetic field \mathcal{R}_B , the maximum redshift out to which these afterglows could be detected with the VLA z_{VLA} , and the peak flux at the redshifted 21 cm frequency, $\nu = 1420/(1+z)$ MHz, for $z \gtrsim 6$,

$$F_{\nu=\frac{1420}{1+z}\text{MHz}}^{\text{peak}} \mu\text{Jy}.$$

model	E [erg]	θ	n [cm $^{-3}$]	p	γ_0	$\frac{T}{1+z}$ [s]	ϵ_e	ϵ_B	\mathcal{R}_B	z_{VLA}	$F_{\nu=\frac{1420}{1+z}\text{MHz}}^{\text{peak}}$ [μJy]
Standard GRB	10^{53}	0.1	0.1	2.2	200	10	0.1	0.01	1	~ 30	1-10
Energetic GRB	10^{54}	0.1	0.1	2.2	200	10	0.1	0.01	1	> 30	10-10 2
High density GRB	10^{53}	0.1	10^2	2.2	200	10	0.1	0.01	1	> 30	10 $^{-1}$ -1
Long duration GRB	10^{53}	0.1	0.1	2.2	200	10^3	0.1	0.01	1	> 30	1-10
Magnetized GRB	10^{53}	0.1	0.1	2.2	200	10	0.1	0.01	5	~ 30	1-10
Hypernova	10^{54}	$1/\sqrt{2}$	0.1	2.2	2	10	0.1	0.01	1	~ 20	10 2 -10 3

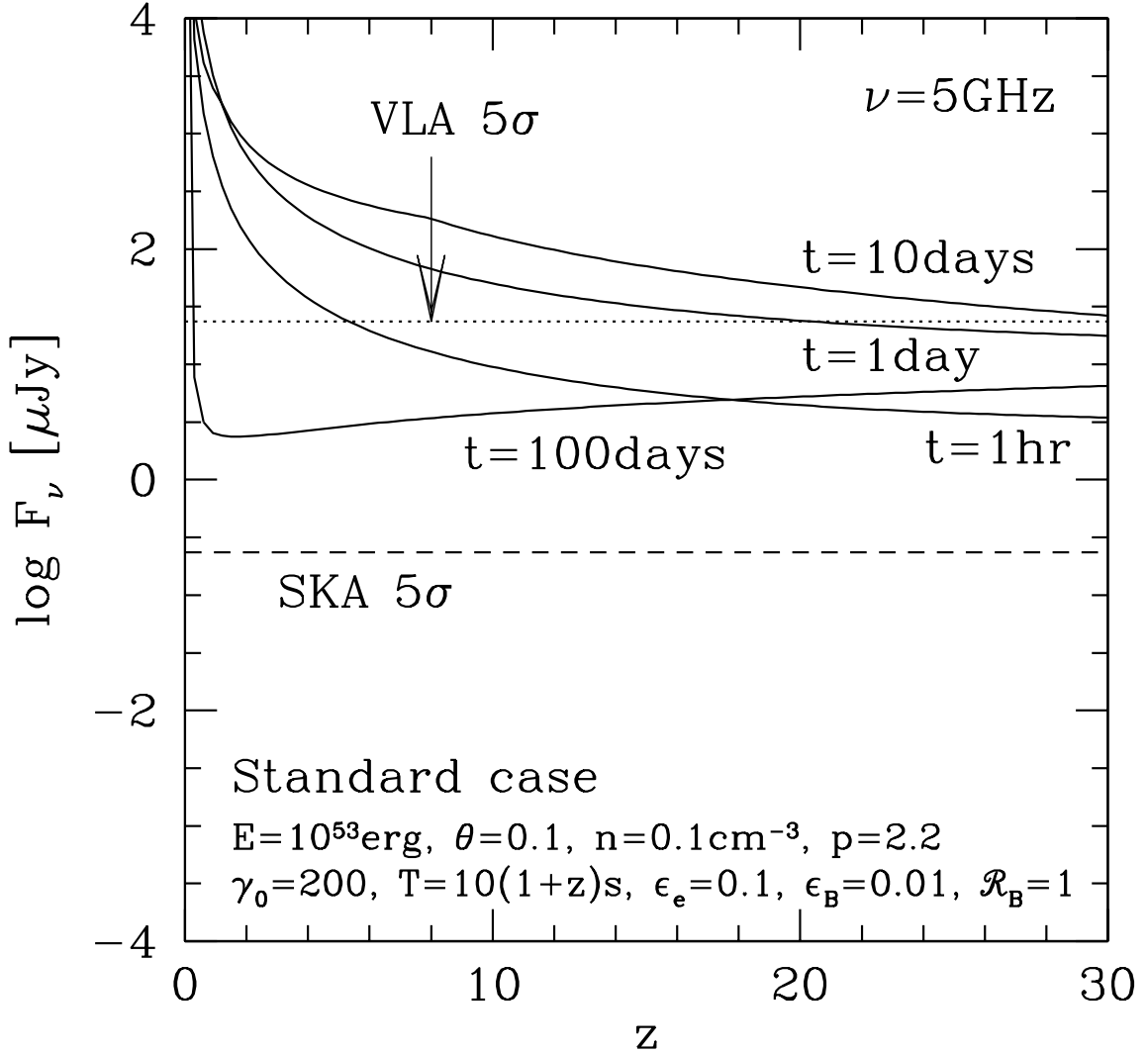


Fig. 1.— GRB afterglow total flux from the forward and reverse shock emission at an observed frequency $\nu = 5$ GHz and observed times 1 hr, 1 day, 10 days and 100 days, as a function of redshift z . The standard model parameters used are: isotropic equivalent energy $E = 10^{53}$ erg, opening half-angle $\theta = 0.1$, ISM density $n = 0.1 \text{ cm}^{-3}$, electron spectral index $p = 2.2$, initial Lorentz factor $\gamma_0 = 200$, GRB duration in the source frame $T/(1+z) = 10$ s, and plasma parameters $\epsilon_e = 0.1$, $\epsilon_B = 0.01$, $\mathcal{R}_B = 1$. The 5σ sensitivities of the VLA (dotted line) and SKA (dashed line) for an integration time $t_{\text{int}} = 1$ day and a band width $\Delta\nu = 50$ MHz are also shown.

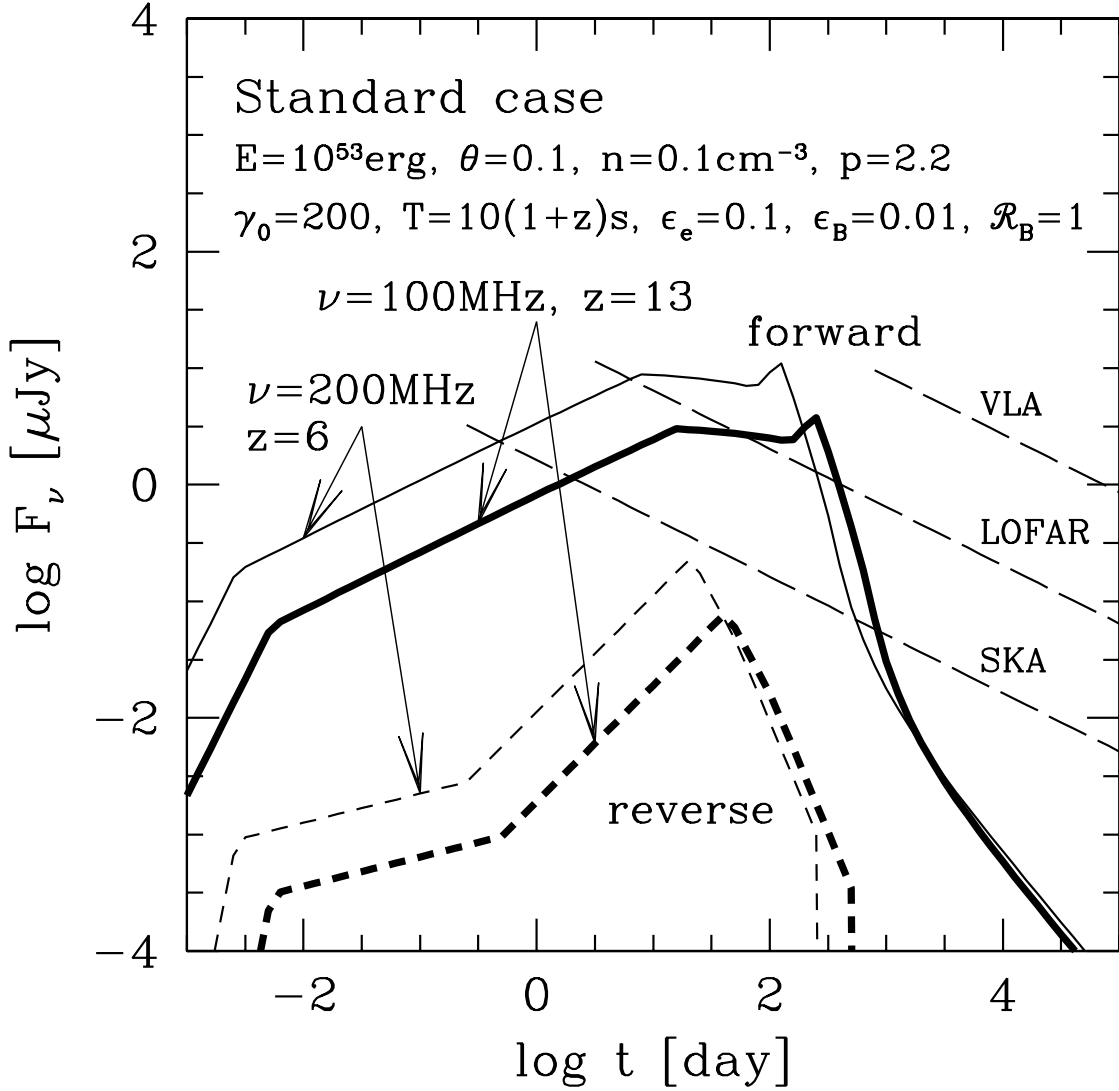


Fig. 2.— GRB afterglow forward shock (solid line) and reverse shock (dashed line) fluxes, shown as a function of the observed time t at frequencies near the redshifted 21 cm radiation for two representative redshifts. We used the standard GRB model parameters: isotropic equivalent energy $E = 10^{53}$ erg, opening half-angle $\theta = 0.1$, ISM density $n = 0.1 \text{ cm}^{-3}$, electron spectral index $p = 2.2$, initial Lorentz factor $\gamma_0 = 200$, GRB duration in the source frame $T/(1+z) = 10$ s, and plasma parameters $\epsilon_e = 0.1$, $\epsilon_B = 0.01$, $\mathcal{R}_B = 1$. The thin lines are for a redshift $z = 6$ and observed frequency $\nu = 200$ MHz, while thick lines are for $z = 13$ and $\nu = 100$ MHz. The 5σ sensitivities of the VLA, LOFAR and SKA for integration times of one-third of t and band width $\Delta\nu = 50$ MHz are also shown by the long dashed lines.

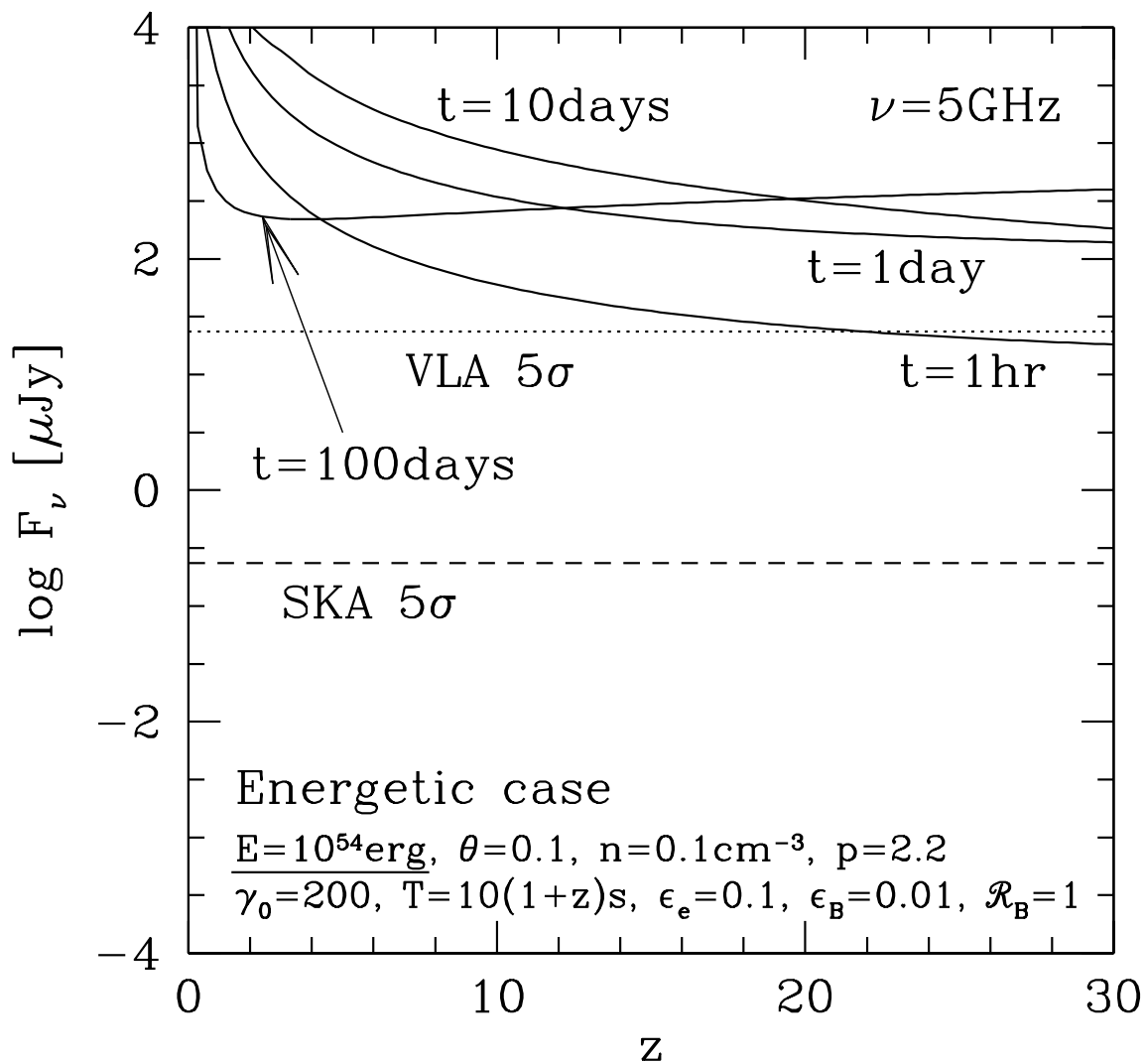


Fig. 3.— GRB afterglow fluxes, same as in Figure 1 except for the isotropic equivalent energy, which is taken here as $E = 10^{54}$ erg.

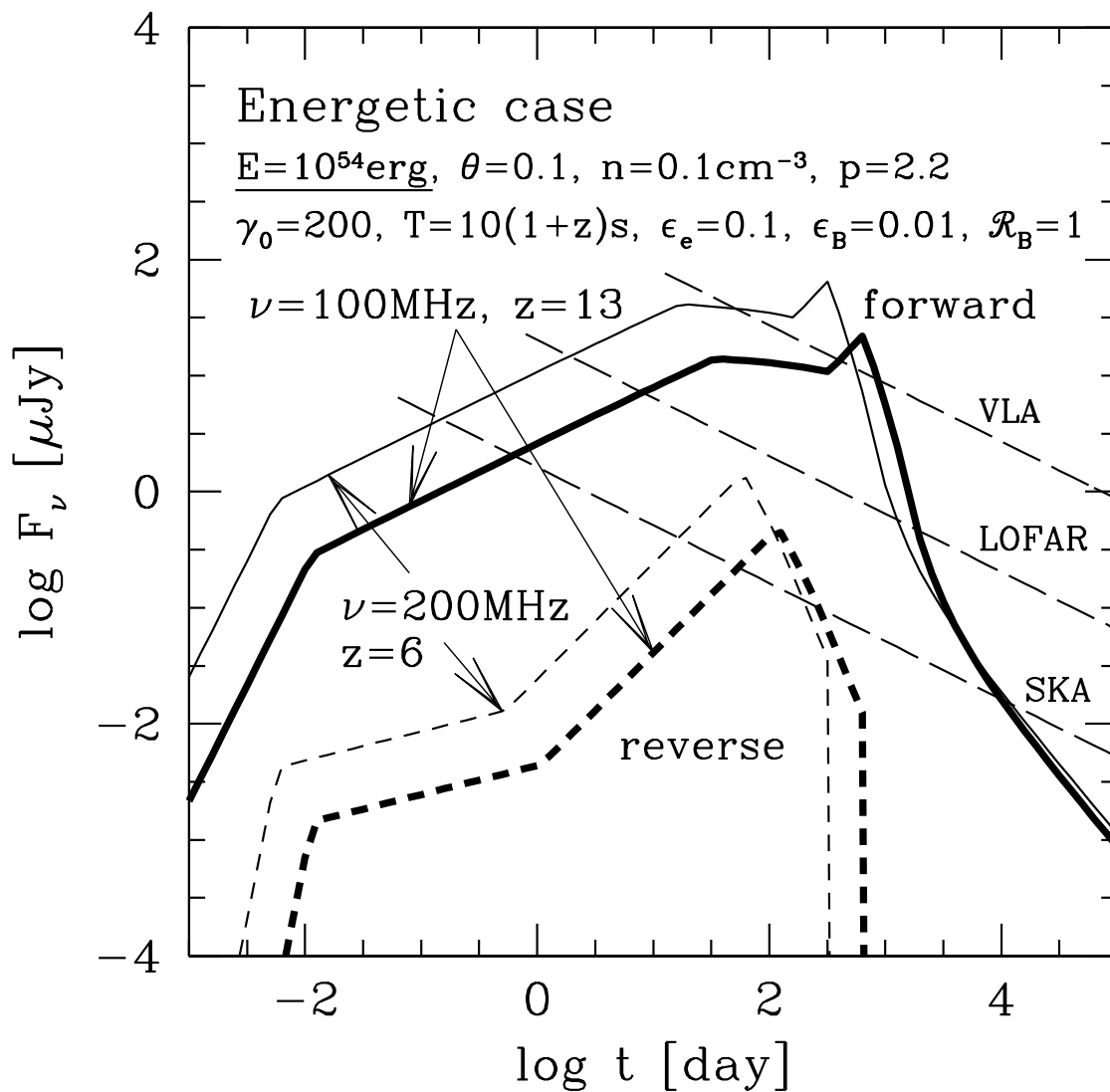


Fig. 4.— GRB afterglow fluxes at two redshifted 21 cm frequencies, as in Figure 2 except for the isotropic equivalent energy, which is taken here as $E = 10^{54}$ erg.

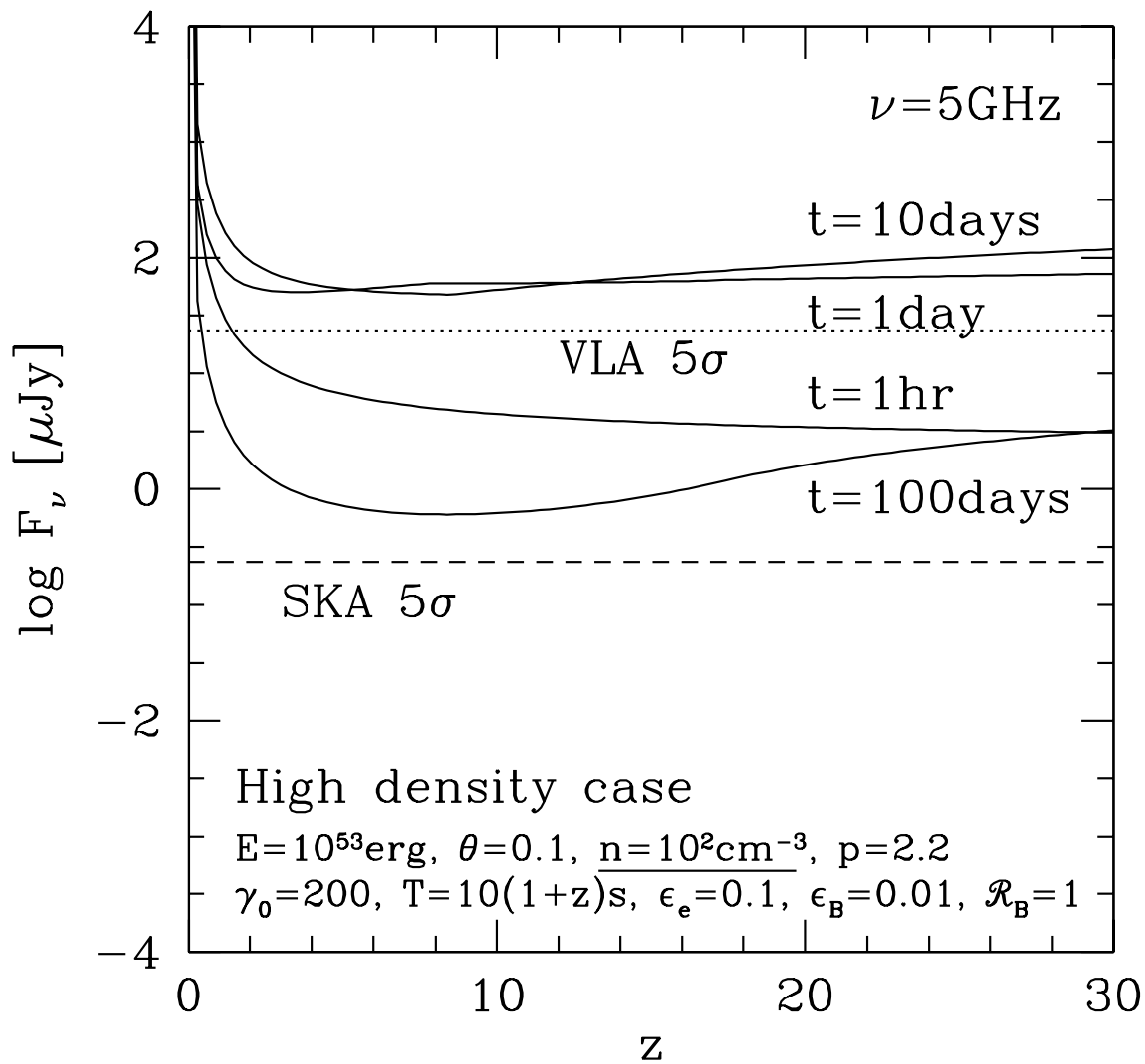


Fig. 5.— GRB afterglow fluxes as in Figure 1 except for the ISM density, which is taken here as $n = 10^2 \text{ cm}^{-3}$.

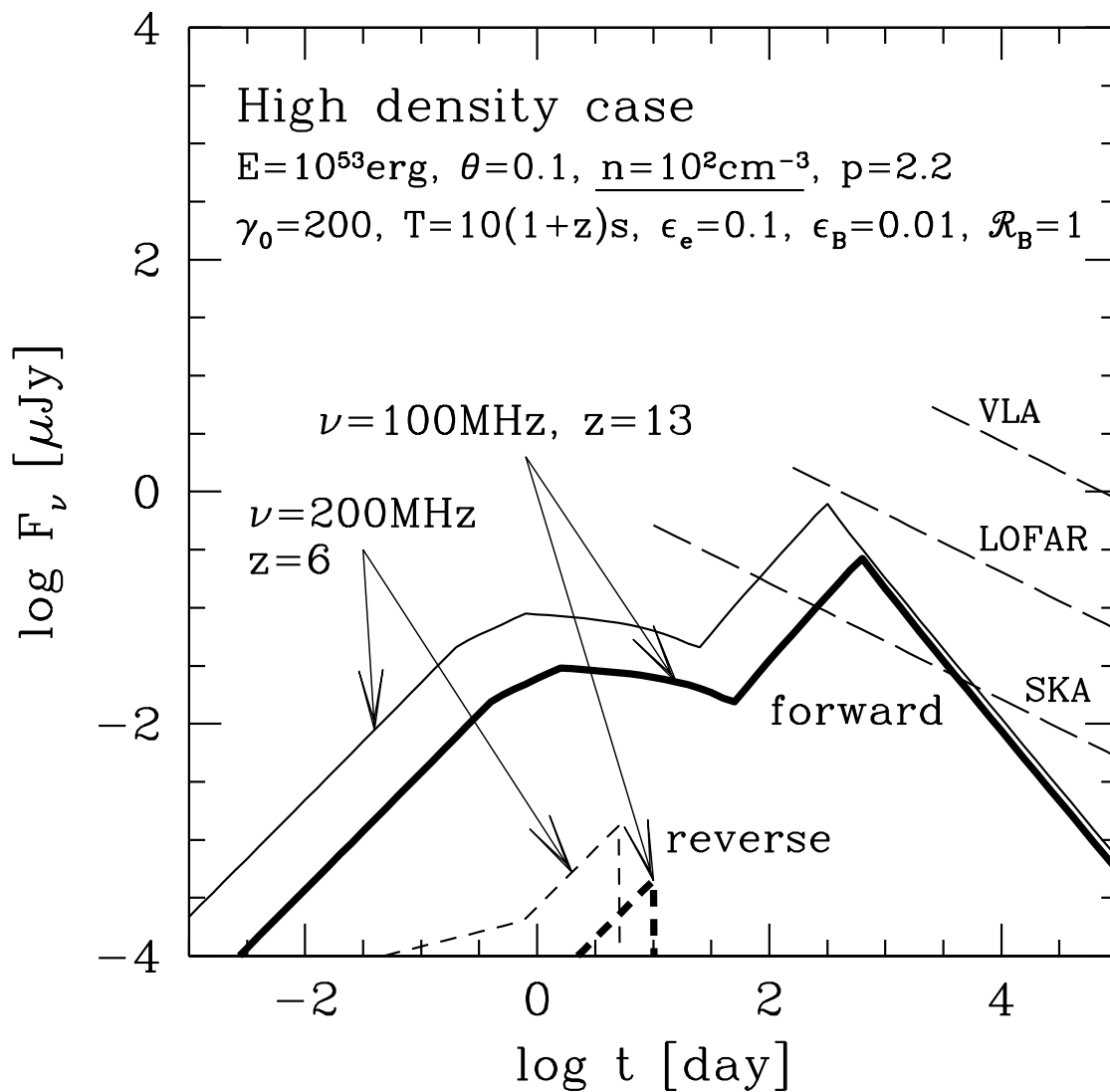


Fig. 6.— GRB afterglow fluxes at two redshifted 21 cm frequencies, as in Figure 2 except for the ISM density, which is taken here as $n = 10^2 \text{ cm}^{-3}$.

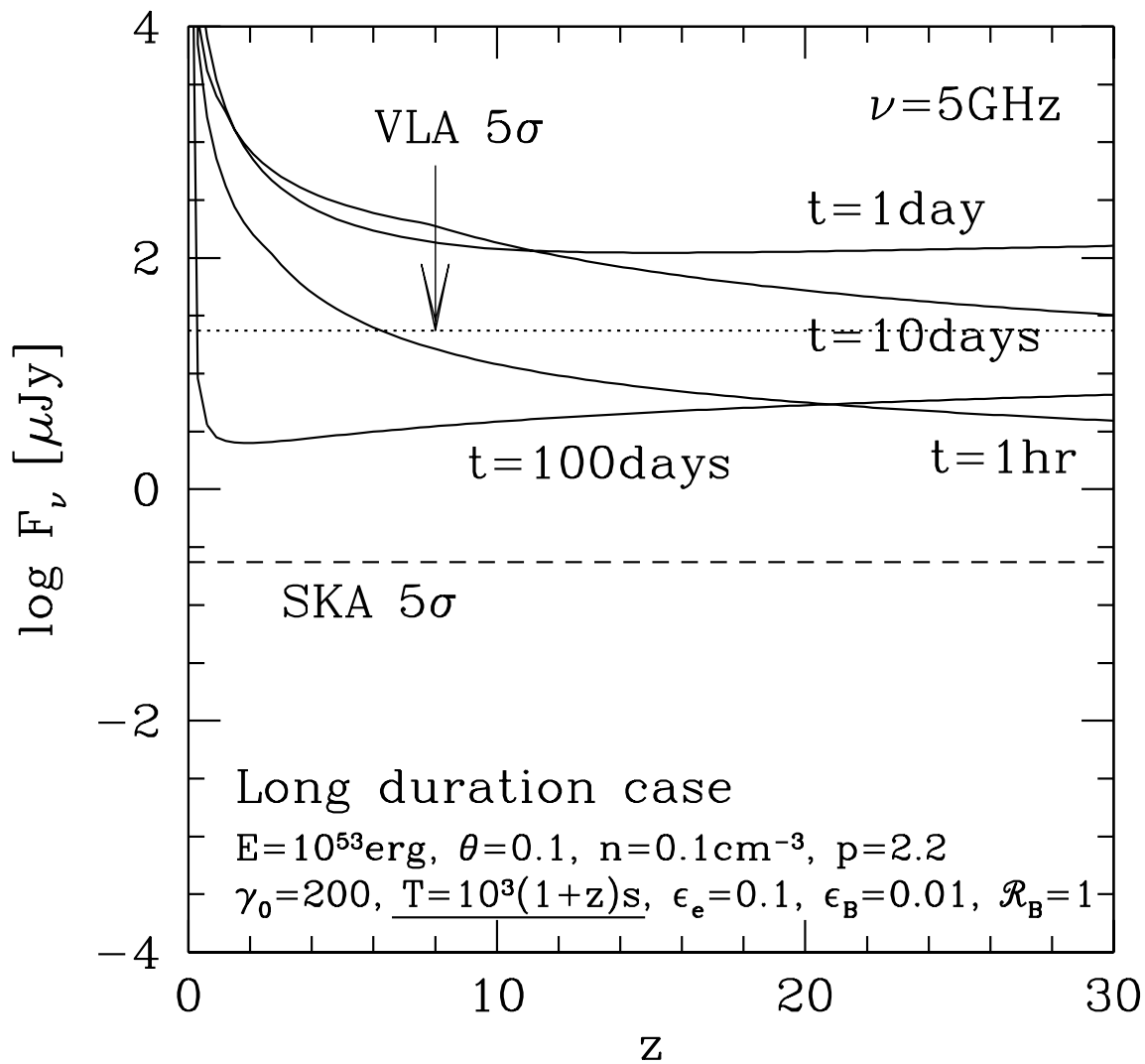


Fig. 7.— GRB afterglow fluxes as in Figure 1 except for the GRB duration in the source frame, which is taken here as $T/(1+z) = 10^3$ s.

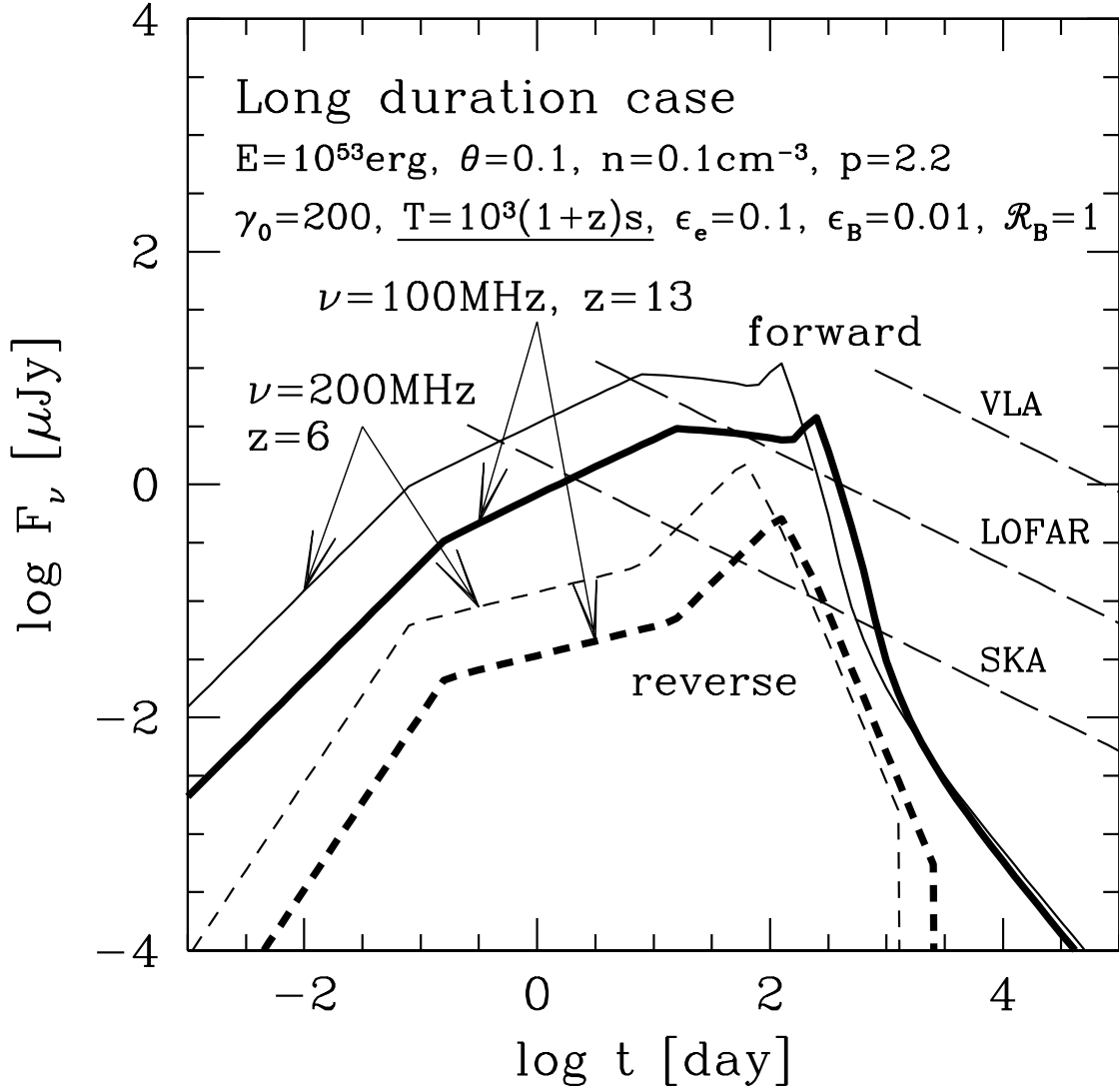


Fig. 8.— GRB afterglow fluxes at two redshifted 21 cm frequencies, same as in Figure 2 except for the GRB duration in the source frame, which is taken here as $T/(1+z) = 10^3$ s.

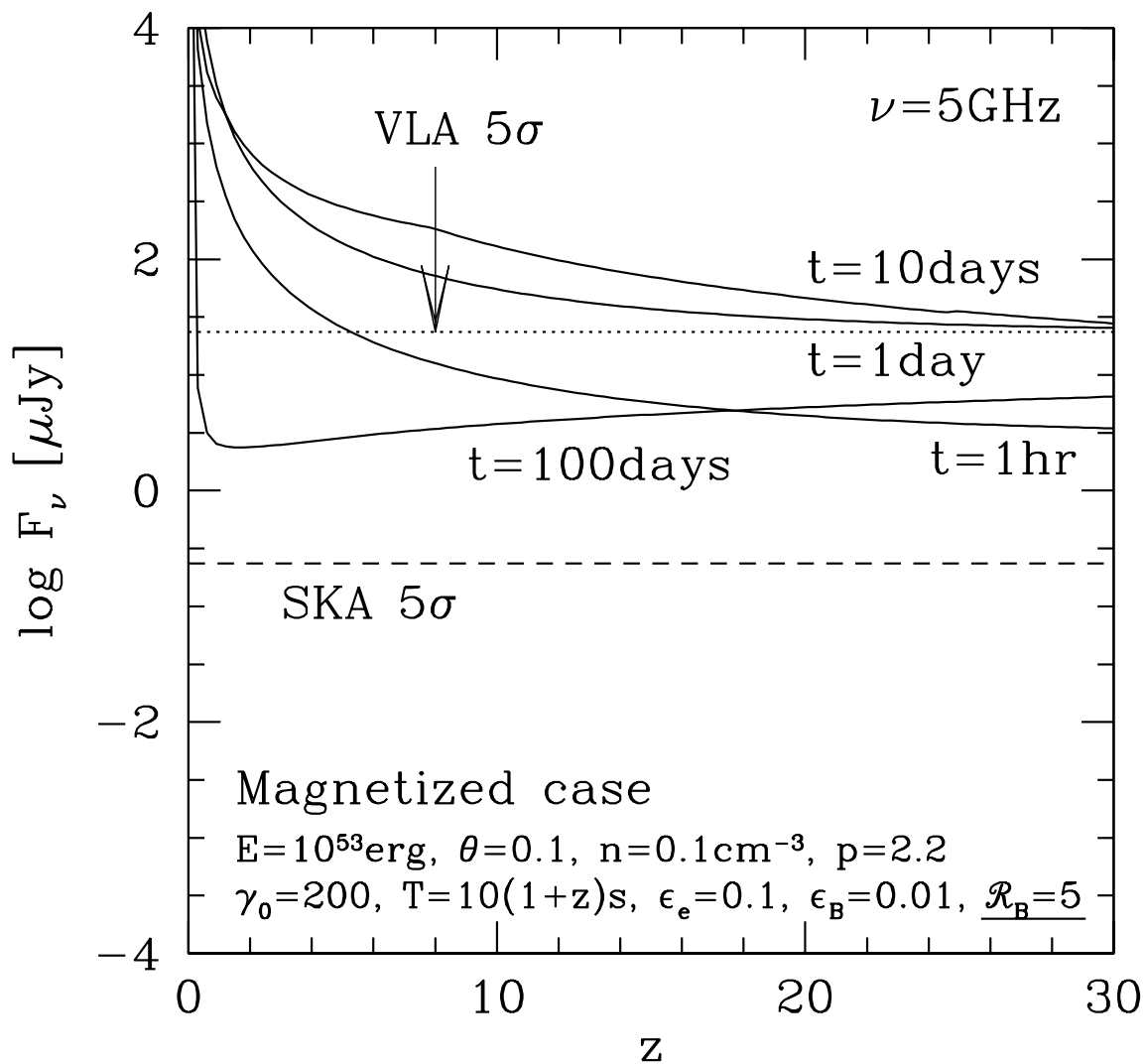


Fig. 9.— GRB afterglow fluxes, as in Figure 1 except for the magnetic field in the reverse shock, which is taken here as $\mathcal{R}_B = (\epsilon_{B,r}/\epsilon_{B,f})^{1/2} = 5$.

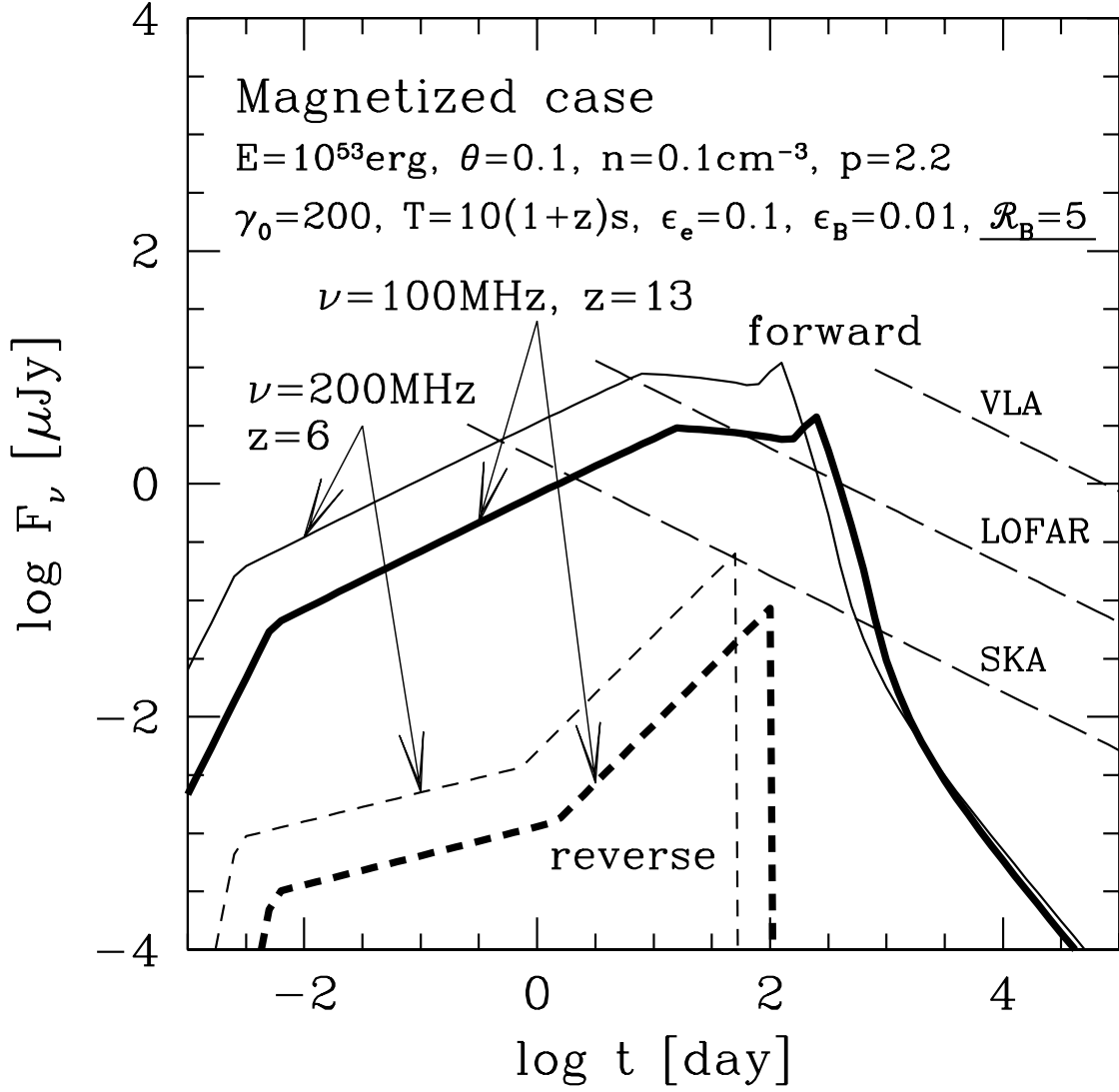


Fig. 10.— GRB afterglow fluxes at two redshifted 21 cm frequencies, as in Figure 2 except for the magnetic field in the reverse shock, which is taken here as $\mathcal{R}_B = (\epsilon_{B,r}/\epsilon_{B,f})^{1/2} = 5$.

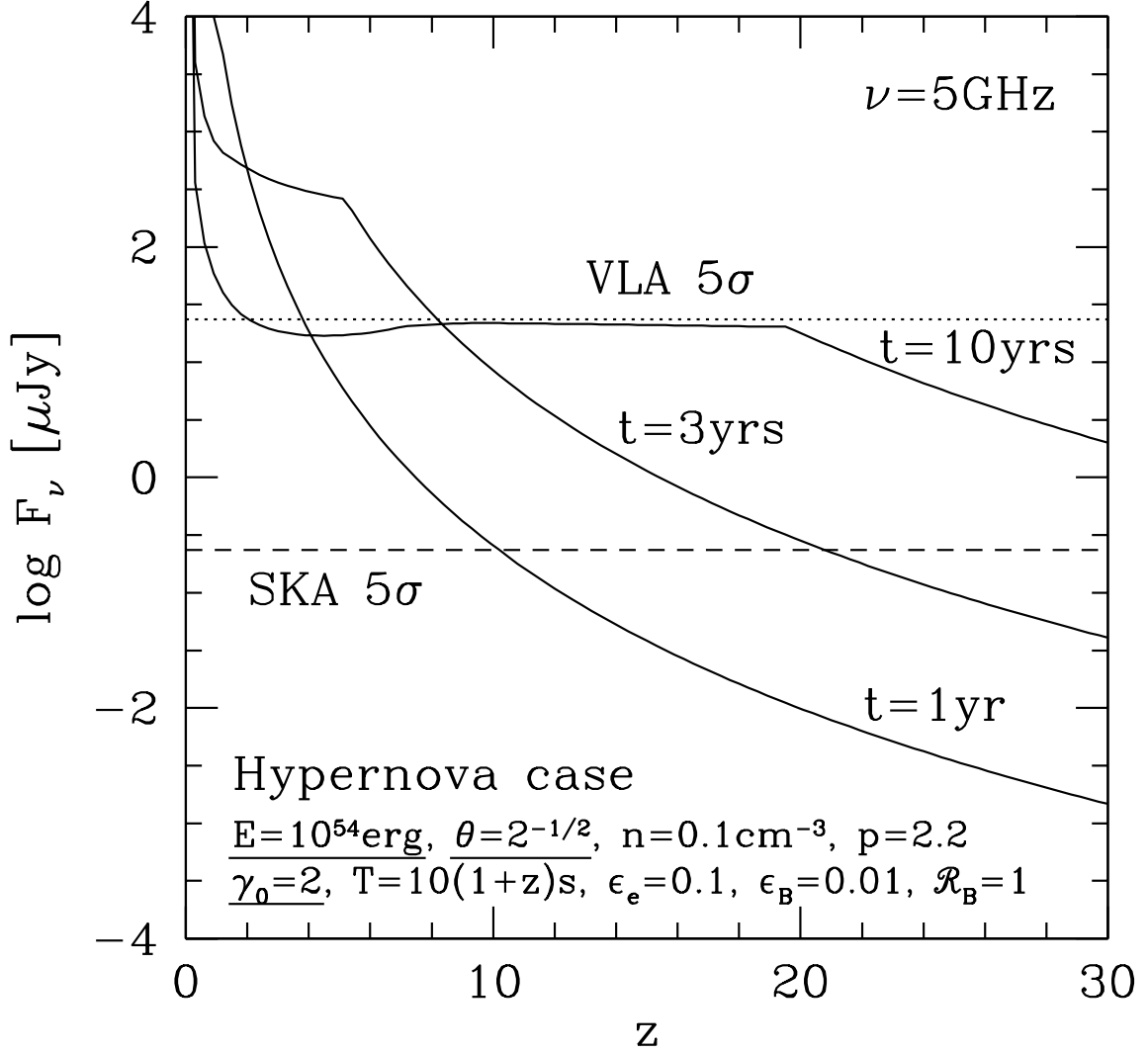


Fig. 11.— Hypernova (HN) remnant total flux from the forward and reverse shock at the observed frequency $\nu = 5 \text{ GHz}$ and observed times 1 yr, 3 yrs and 10 yrs, shown as a function of redshift z . The model parameters are as for the standard GRB case in Figure 1, except for the isotropic equivalent energy $E = 10^{54} \text{ erg}$, the opening half-angle $\theta = 2^{-1/2}$ (nearly spherical) and the initial Lorentz factor $\gamma_0 = 2$ (mildly relativistic). The 5σ sensitivities of the VLA (dotted line) and SKA (dashed line) for an integration time $t_{\text{int}} = 1 \text{ day}$ and a band width $\Delta\nu = 50 \text{ MHz}$ are also shown.

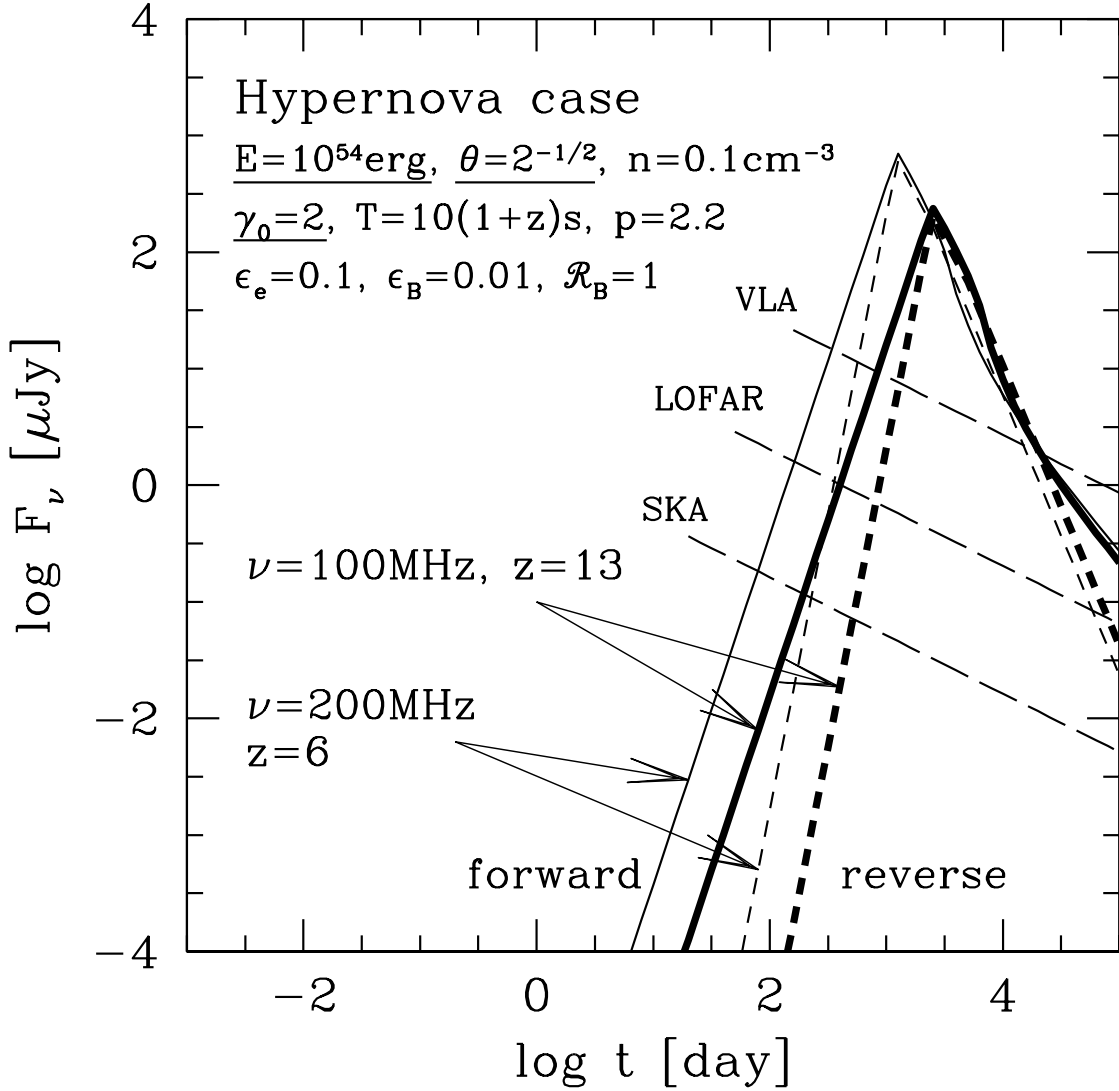


Fig. 12.— Hypernova (HN) remnant fluxes at two redshifted 21 cm frequencies, same as Figure 2 except for the isotropic equivalent energy $E = 10^{54}$ erg, the opening half-angle $\theta = 2^{-1/2}$ (nearly spherical) and the initial Lorentz factor $\gamma_0 = 2$ (mildly relativistic). The 5σ sensitivities of the VLA, LOFAR and SKA for the integration time of one-third of t and the band width $\Delta\nu = 50$ MHz are also shown by the long dashed lines.